# Investigating the emission properties of plasma structures with x-ray imaging spectroscopy

I. Yu. Skobelev, A. Ya. Faenov, B. A. Bryunetkin, and V. M. Dyakin

*All-Russia Scientific Research Institute of Engineering Physics and Radio Engineering Measurements, 141570 Mendeleevo, Moscow District, Russia*

T. A. Pikuz

*N. É. Bauman State Technical University, 107059 Moscow, Russia*

S. A. Pikuz, T. A. Shelkovenko, V. M. Romanova, and A. R. Mingaleev

*P. N. Lebedev Institute of Physics, Russian Academy of Sciences, 117924 Moscow, Russia*
(Submitted 15 March 1995)
Zh. Éksp. Teor. Fiz. **108**, 1263–1308 (October 1995)

A new class of instruments for x-ray spectroscopy has emerged, especially for imaging x-ray spectroscopy, comprising fast spectrographs with spherical crystals, transmission diffraction grating-obscurae, and multilayer Fresnel lenses. These instruments significantly extend the capabilities of experimental spectroscopy of high temperature plasmas. In this paper we show that the use of these instruments in the atomic spectroscopy of multiply charged ions greatly improves the accuracy of measurements of x-ray spectral line wavelengths, and makes possible the study of previously unobserved low-intensity spectral transitions. In addition, their use in plasma diagnostics yields information about one- and two-dimensional spatial parameter distributions both of nonuniform plasma microsystems (e.g., micropinches, or dense regions of a laser plasma) and extended plasma sources in regions of low luminosity (e.g., freely expanding laser plasmas at large distances from the target). We present here the results of our experimental and theoretical studies of the radiative properties of real plasma objects (i.e., *X* pinch, *Z* pinch with composite loading, and plasmas produced by laser pulses with nanosecond and subpicosecond durations). © *1995 American Institute of Physics.*

## 1. INTRODUCTION

X-ray spectroscopy of multiply charged ions is presently one of the most powerful techniques available for investigating high temperature plasmas. Indeed, x-ray spectroscopic methods have thus far provided most of our information on parameters of both laboratory and astrophysical plasmas, and on the processes that take place within them (see, e.g., the reviews and monographs Refs. 1–6).

In recent years, new classes of x-ray spectroscopic instruments have appeared whose members possess not only dispersive, but focusing properties as well. Such instruments enable us not only to investigate the spectral composition of the x-ray emission but also to image plasma objects in spectral lines. Their principal advantage over more traditional instruments is that they combine very high speed with high spatial resolution, while preserving the highest possible spectral resolution of their dispersive element. Using these instruments, it is possible, first of all, to obtain more detailed information about the properties of previously studied plasma sources, and secondly, to investigate in detail a number of relatively new plasma laboratory objects with very small dimensions (e.g., micropinches) or low energy content (plasmas produced by subpicosecond laser pulses). In Sec. 2 of this paper we discuss these new instruments for x-ray imaging spectroscopy; in Secs. 3 and 4, respectively, we present results of experiments in which these instruments were used for atomic spectroscopy of multiply charged ions and high-temperature plasma diagnostics.

## 2. X-RAY SPECTROSCOPY OF PLASMA OBJECTS: ONE- AND TWO-DIMENSIONAL SPATIAL RESOLUTION

### 2.1. Bragg x-ray spectroscopic instruments

In this section, we discuss imaging of plasma objects in individual spectral lines using spectrographs with crystals as their dispersive elements. Because crystals are highly dispersive, these instruments enable us to record images with high spatial resolution and good spectral selectivity. With their good characteristics, these objects are distinguished by simplicity of design and convenience of alignment, which are very important in complex experiments where the installation of a large amount of diagnostic equipment usually presents problems.

In these various spectrographic schemes, images are obtained by using plane or cylindrically curved crystals (both concave and convex), as well as crystals that conform to second-order surfaces, e.g., spherical. Depending on the problems addressed by the experiment, each of these spectrographs can generate images with both one- and two-dimensional spatial resolution. When used in this way, they are characterized by the following parameters, which are the most important for investigating plasma objects: spectral and spatial resolution, spectral detection range, and speed (i.e., focal ratio).

In what follows, we discuss those instruments that are of interest with regard to practical use in various experiments

 1063-7761/95/100692-27$10.00 © 1995 American Institute of Physics 

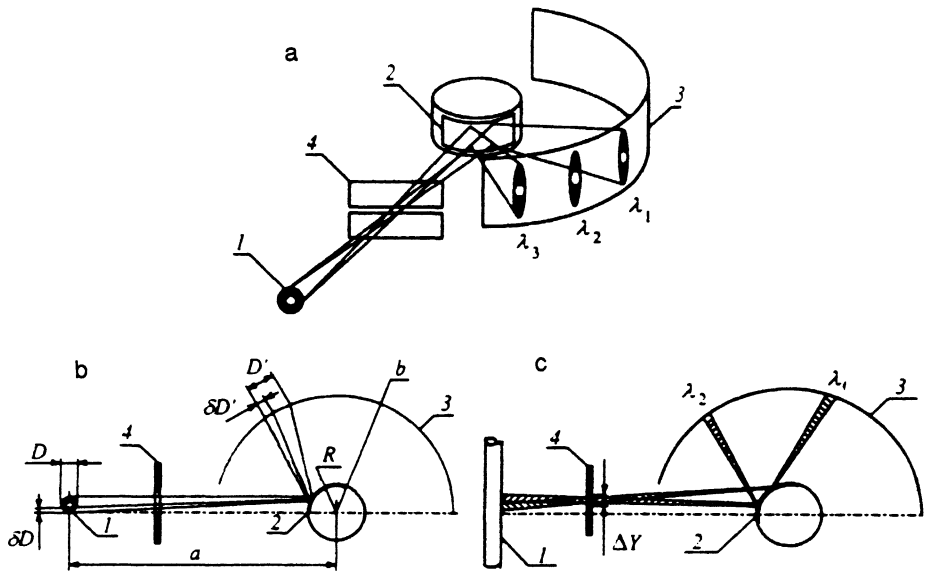


FIG. 1. Defocusing spectrograph with spatial resolution. (a) Elements of the spectrograph. (b)Spatial resolution when the slit is parallel to the direction of dispersion. (c) Scheme for obtaining good spatial resolution in the radial direction of an extended source. *1*—source; *2*—crystal; *3*—photographic film; *4*—slit; *a*—distance from source to the axis of curvature of the crystal; *b*—distance from axis of curvature of the crystal to the image; *D*—diameter of the source; *R*—radius of curvature of the crystal.

involving the recording of spectrally selective images of plasma objects.

#### *2.1.1. Defocusing spectrographs*

Defocusing spectrographs are characterized by the highest spectroscopic field of view. Therefore, despite their low speed and spectral resolution, they can be used successfully to investigate extended high-intensity plasma objects with complicated internal structure.

The layout of a defocusing spectrograph in shown in Fig. 1a. In accordance with the Bragg condition, we have

$$m\lambda = 2d \sin \theta, \tag{1}$$

where $\lambda$ is the wavelength of the x rays, $d$ is the distance between crystallographic planes of the crystal, $\theta$ is the Bragg angle, and $m$ is the diffraction order. In this scheme, the spectral range of the detected x rays for each reflection order lies within the full range of wavelength variation from $\lambda = 0$ (for $\theta = 0°$, i.e., the incident ray is tangent to the crystal) to $\lambda \approx 2d/m$ (for $\theta = 90°$, i.e., normal incidence). In this case, the spectrograph possesses spatial resolution in the direction of dispersion.

To obtain a two-dimensional image of a source, a slit is positioned between the source and the crystal, oriented parallel to the dispersion. The linear magnification of this image differs in the two principal directions: in the direction of dispersion, we have a magnification of $\beta_1 \simeq b/a$, where $a$ and $b$ are the respective distances from the source to the center of curvature of the crystal and from the center of curvature of the crystal to the photographic film, while perpendicular to the dispersion the magnification equals $\beta_2 = p/q$, where $q$ is the distance from the source to the slit, and $p$ is the distance from the slit to the film.

Spatial resolution perpendicular to the dispersion depends on the width of the slit, and is limited by the diffraction of x rays. By reducing the dimensions of the slit, we can obtain resolutions down to 10–20 $\mu$m. Here it is necessary to take into account that the slit acts as an aperture for the x rays, and its minimum size is limited by the achievable speed of the instrument. In the direction of dispersion (Fig. 1b), the spatial resolution at the photographic film is

$$\delta D' = 2a' \left( \frac{\Delta\lambda}{\lambda} \tan \theta + \delta\theta \right), \tag{2}$$

where $a$ is the distance from the source to the center of curvature of the crystal, and $\delta\theta$ is the width of the rocking curve of the crystal.

In Eq. (2), the first term in parentheses represents the influence of spectral broadening of the source line, while the second is the broadening due to the rocking curve of the crystal. It follows from Eq. (2) that to increase the spatial resolution it is necessary to reduce the distance from the source to the crystal as much as possible. Spatial resolution in such a scheme usually does not exceed 100 $\mu$m in the plane of dispersion.

This scheme exhibits several peculiarities when used to investigate extended linear sources, e.g., in experiments involving linear compression (see Fig. 1c). To study the fine radial structure of an object, the slit of the instrument must be parallel to the axis of the extended object. In this case, the slit, as before, should be parallel to the dispersion; the axis of a convex crystal must therefore be rotated by an angle of 90° relative to the axis of the object. However, this causes the spectral resolution to drop sharply due to the large dimensions of the source. It is possible to obtain acceptable spectral resolution while preserving good spatial resolution in the radial direction by stopping down the slit in the direction of dispersion. Different portions of the objects will then be imaged in different spectral lines. For a uniform plasma source, this has no effect on the results. For other types of sources, not only must it be allowed for, it can actually be employed to address novel research problems.

In our experiments we used both types of defocusing spectrograph schemes. In Sec. 4, we describe the most interesting results obtained in recording two-dimensional spec-

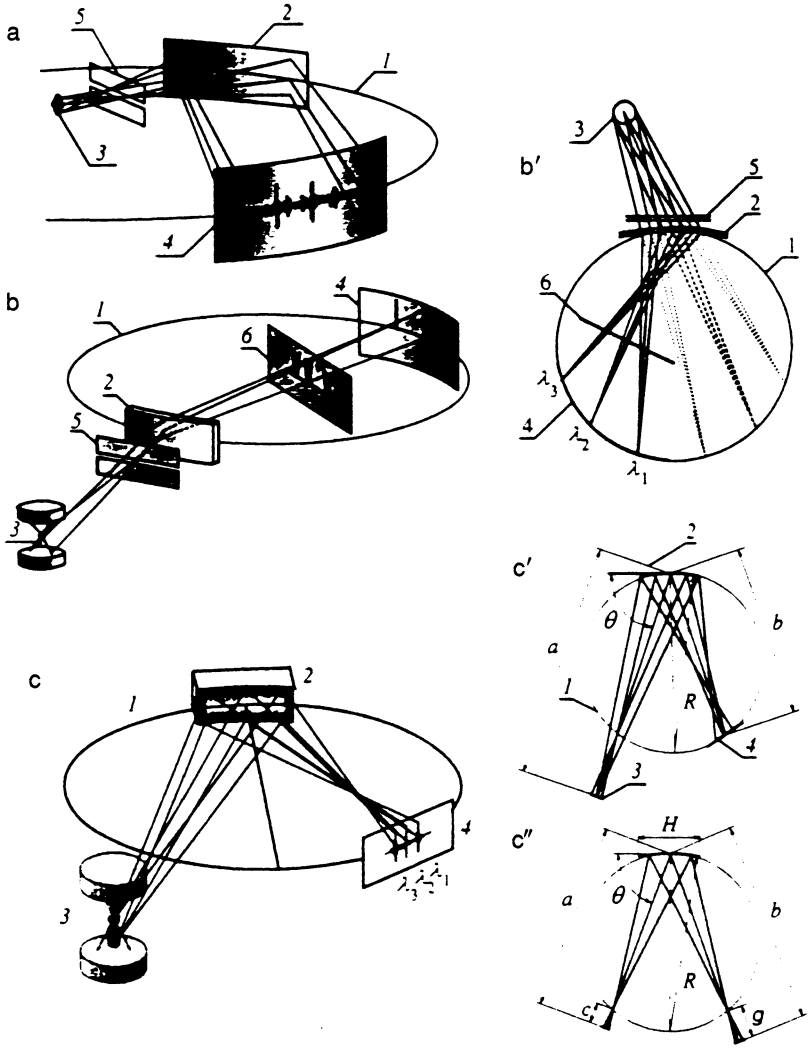


FIG. 2. Focusing crystal spectrographs: *a*—Johann spectrograph with a slit; *b*—Cauchois spectrograph with a slit, *b′*—ray path in the Cauchois spectrograph; *c*—FSPR-1 spectrograph, *c′*—ray path in the meridional plane of the FSPR-1 spectrograph, *c″*—ray path in the meridional plane of the FSPR-2 spectrograph: *1*—Rowland circle; *2*—crystal; *3*—source; *4*—image; *5*—slit; *6*—photographic film; *a*—distance from crystal to source; *b*—distance from crystal to image; *R*—radius of curvature of the crystal; *H*—size of crystal in the meridional plane.

trally selective images of plasmas generated by the compression of "liners" in the large-scale *Angara 5* experiment.

#### *2.1.2. Focusing spectrographs with cylindrical crystals*

Two members of the class of focusing spectrographs with cylindrical crystals are the Johann spectrograph, in which x rays are selectively reflected from the interior (concave) crystal surface (Fig. 2a), and the Cauchois spectrograph, in which the crystal operates in transmission (Fig. 2b). In contrast to defocusing instruments, these spectrographs have a considerably smaller spectroscopic field of view, but their speed and spectral resolution are considerably higher.

Because Johann spectrographs have traditionally been used for x-ray spectroscopy of plasma objects (see, e.g., Ref. 1), we will not dwell on the details of this scheme. Instead, we will concentrate on the distinctive features of the Cauchois spectrograph. This type of spectrograph is of great interest as a means of recording x rays in the short-wavelength region of the spectrum $\lambda<3$ Å, because in this range the reflectivity of most crystals falls off abruptly.

In the Cauchois spectrograph (Fig. 2b), the source of x rays is positioned on the Rowland circle in such a way that the x rays pass through the curved crystal located on the circle, and are focused onto photographic film also located on the circle. The linear dispersion in this scheme is

$$D_x=\frac{\lambda}{R}\cot\theta, \tag{3}$$

where $R$ is the radius of curvature of the crystal. The spectral resolution is given by

$$M=\frac{\lambda}{\Delta\lambda}\,\frac{R}{l^2/8R+p}, \tag{4}$$

where $p$ is the crystal thickness and $l$ is the size of the working region of the crystal for a given wavelength.

Because the size of the working region depends on the dimensions of the source, it follows from (4) that for a small source (a situation typical of most experiments), the spectral resolution is determined solely by the ratio of the radius of curvature to the crystal thickness. This makes it possible to obtain spectral resolutions from 1000 to 10000.

Just as in the defocusing spectrographs discussed in Sec. 2.1.1., using a slit positioned parallel to the direction of dispersion makes it possible to record spectra with spatial resolution. In Fig. 2b we show that when the slit *5* is positioned between the source *3* and crystal *2*, a spectrally selected image of the plasma with one-dimensional spatial resolution is

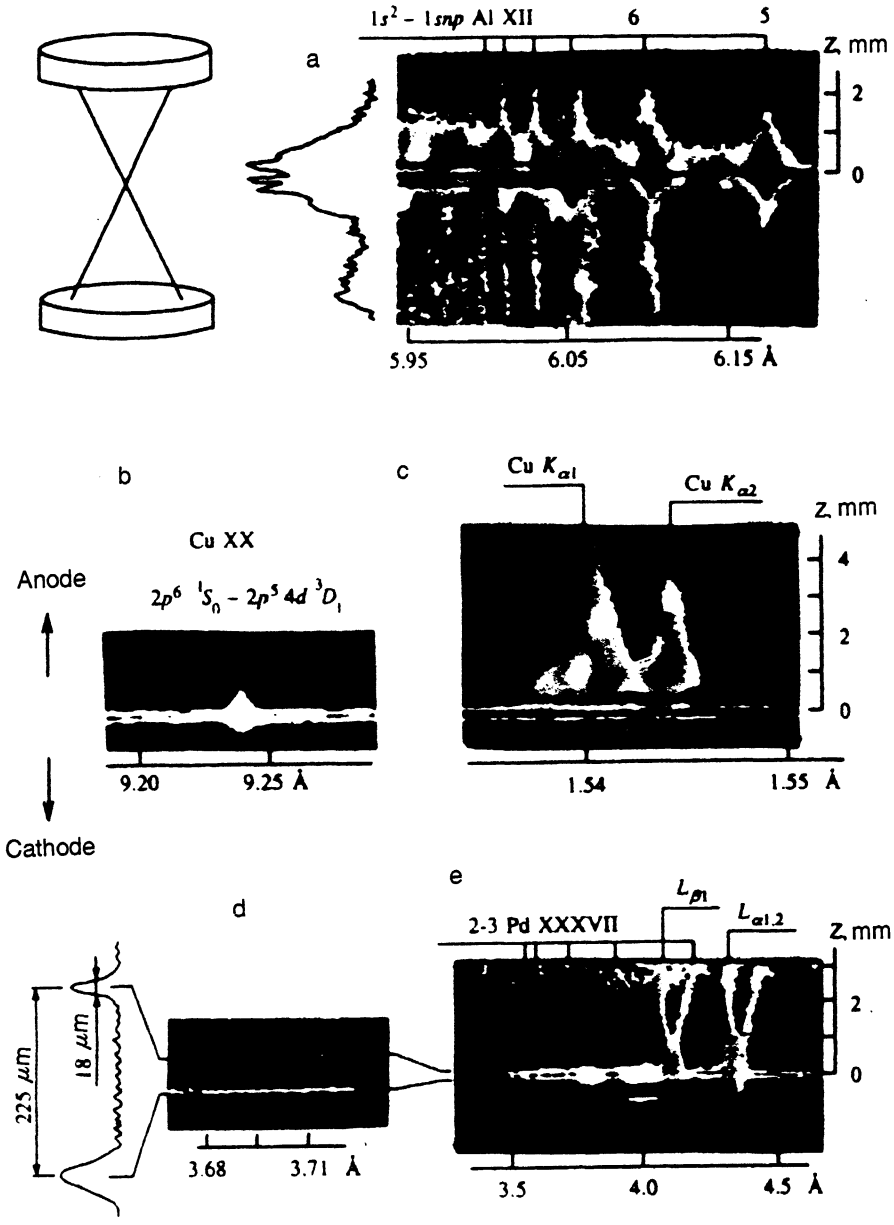


FIG. 3. Image of an *X*-pinch plasma in *K* and *L* spectral lines: a) spectrum of He-like Al recorded from three hot spots of the *X* pinch using an FSPR-1 spectrograph; b, c) spectrum of Ne-like copper (2nd reflection order) and $K\alpha_1$, $K\alpha_2$ lines of Cu (7th reflection order), recorded simultaneously with an FSPR-1 spectrograph; d) spectrogram of continuum x rays from hot spots of the *X* pinch (of a palladium wire), demonstrating the high spatial resolution of the FSPR-1 spectrograph (using a mica crystal with $R=100$ mm, 5th reflection order); e) *L* spectrum of palladium recorded by a spectrograph with a convex CsAP crystal.

obtained on the photographic film *4* located on the Rowland circle. When the film is positioned outside the Rowland circle (position *6* in Fig. 2b), the plasma is imaged with two-dimensional spatial resolution. Experimental results obtained using the Cauchois scheme in various configurations are also discussed in Sec. 4.

### 2.1.3. Focusing spectrographs with spherical crystals

By using focusing spectrographs in which a spherically curved crystal is used as the dispersive element, we can greatly increase the instrument's speed over that obtainable with cylindrical crystals due to the focusing of the x rays in the plane perpendicular to the dispersion.

*2.1.3.1. Focusing spectrographs with one-dimensional spatial resolution (FSPR-1).* Figure 2c shows a focusing spectrograph with one-dimensional spatial resolution. In the plane of the Rowland circle, which we will refer to as the meridional plane, this setup operates like an ordinary Johann spectrograph with all of its advantages with regard to spectral resolution and speed. In the plane perpendicular to the meridional plane, which we will refer to as the sagittal plane, it operates as an ordinary mirror, focusing x rays in this direction, and making it possible to significantly increase the speed of the instrument.

For nonnormal Bragg angles, this scheme suffers from astigmatism, so meridional and sagittal rays focus differently: spectral focusing takes place in the meridional plane, while spatial focusing takes place in the sagittal plane. The distance from the center of the crystal to the sagittal focus is given approximately by

$$f_s = R/2 \sin\theta. \tag{5}$$

Equation (5) implies that best focus is achieved when the source *3* is a distance $a=R\cos\varphi/\cos 2\varphi$ from the crystal *2*, and the photographic film *4* is located on the Rowland circle at a distance $b=R\cos\varphi$ from the crystal (Fig. 2c′). Here

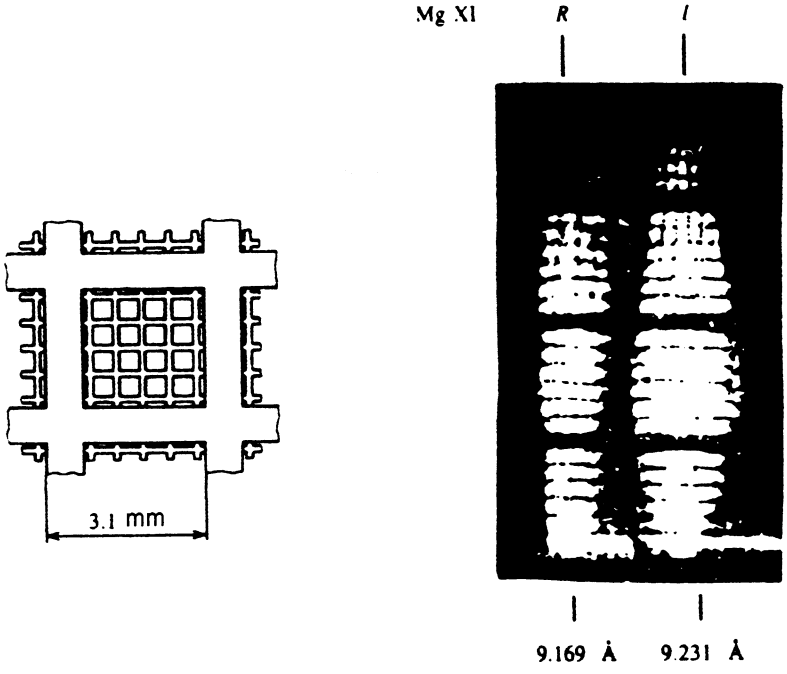


FIG. 4. Image of two grids superimposed on one another (with wire diameters 100 and 500 $\mu$m) obtained in laser plasma light, using an FSPR-2 spectrograph with a spherical mica crystal with a radius of 100 mm. $R$, $I$ are the $1s^2\ {}^1S_0-1s2p\ {}^1P_1$ and $1s^2\ {}^1S_0-1s2p\ {}^1P_1$ resonance and intercombination lines of the He-like Mg XI ion.

$\varphi=90°-\theta$ is the angle of incidence of the x rays on the crystal. In this case, the linear magnification $\beta$ in the plane of the film is

$$\beta=\frac{b}{a}=\cos 2\varphi=2(m\lambda/2d)^2-1. \tag{6}$$

Due to the focusing of the x rays in the sagittal plane, spherical spectrographs are very fast. A comparison of the speed of spherical spectrographs with Johann spectrographs shows that the former are

$$G=[1-2a\ \sin\ \theta/(a+R\ \sin\ \theta)]^{-1} \tag{7}$$

times faster than the latter. Despite the fact that $G$ is limited by aberrations equivalent to those of a spherical mirror and depends critically on the quality of the crystal, in practice this quantity ranges from 10 to 500.

In this scheme, focus conditions are met in the vicinity of real images produced by the crystal as a spherical mirror. Because the distances $a$ and $b$ are uniquely related through the angle $\varphi$ to the wavelength of the detected x rays, we find from the expression for $a$ that $\varphi$ can range from 0° to 45°. This range of $\varphi$ corresponds to a wavelength range of $2d/m$ to $\sqrt{2}d/m$. For the first reflected order of the crystal, this range is not large. However, in our experiments we used mica crystals with high reflectances in many reflection orders from 1 to 13. This enabled us to experiment over a broad spectral range, from 1.1 Å to 19.94 Å.[7-11]

Spatial resolution in the FSPR-1 scheme is governed by the laws of optics, imperfections in the crystal, and the quality of the spherical surface. From an engineering point of view, producing a high-quality bend with the required radius of curvature in a crystal is a relatively complicated problem. Nevertheless, modern fabrication techniques are sufficiently advanced to enable high-quality large-aperture crystals of mica (10–20×30–70 mm) to be made with $R=100$, 186, 250, and 443 mm. We were therefore able to use crystals with $R=100$ mm in our experimental study of the Pd $X$ pinch, where we obtained spatial resolutions of better than 20 $\mu$m (Fig. 3d).

We discuss other high-precision wavelength measurements and diagnostics of various sources obtained with FSPR-1 spectrographs in Secs. 3 and 4.

*2.1.3.2. Focusing spectrographs with two-dimensional*

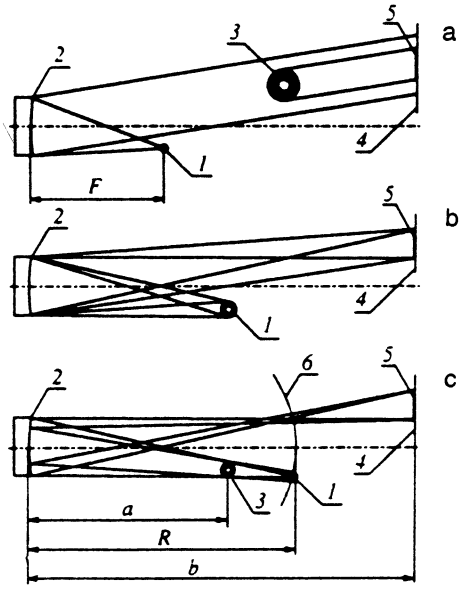


FIG. 5. Optical layout for a spherical crystal mirror: a) to generate a monochromatic collimated beam; b) in the x-ray microscope scheme; c) to obtain a shadow image in the monochromatic x-ray emission of a backlit plasma source. (*1*—emission source; *2*—crystal; *3*—test object; *4*—photographic film; *5*—image; *6*—Rowland circle; $F$—focal length of the mirror, $R$—radius of curvature of the crystal; $a$—distance from mirror to object; $b$—distance from mirror to image.)

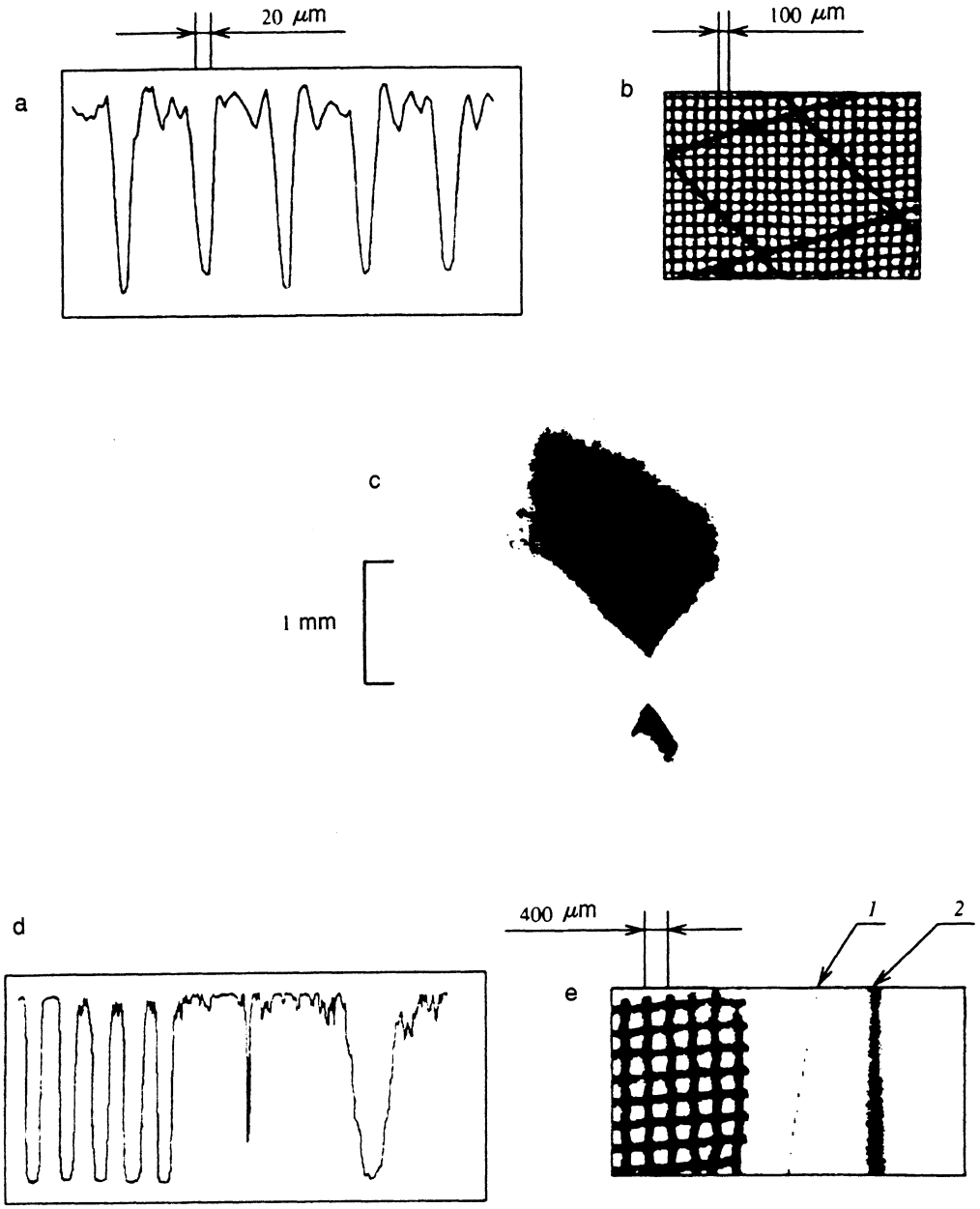


FIG. 6. a) Density and b) shadowgram of a test object obtained in collimated monochromatic x rays from a copper wire $X$ pinch (using a mica crystal with $R=250$ mm); c) image of the $X$-pinch emission source in the $1s^2-1s3p$ line of the He-like Al XII ion; d) Density and e) shadowgram in the $1s^2-1s3p$ line from the He-like Al XII ion of test grids with period 400 $\mu$m, Al wires of diameter 37 $\mu$m, and an expanding plasma obtained by exploding an Al wire of the same diameter.

*spatial resolution (FSPR-2).* FSPR-2 spectrographs are used to obtain two-dimensional spectrally selective images. A sketch of such a spectrograph is shown in Fig. 2c″. From the figure, it is clear that the FSPR-2 and FSPR-1 spectrographs differ only in the position of the photographic film: in the latter case, it is located outside the Rowland circle.

Let us consider the basic relations that hold in this spectrograph scheme. In accordance with the laws of geometrical optics in the sagittal plane, the position of the source relative to the crystal (distance $a$) and the photographic film relative to the crystal (distance $b$) are related by

$$\frac{1}{a}+\frac{1}{b}=\frac{1}{f_s}, \tag{8}$$

where $f_s=R/2\sin\theta$ is the sagittal focal length. This yields the linear magnification in the sagittal plane:

$$G=\frac{b}{a}=\frac{R}{2a\ \sin\ \theta-R}. \tag{9}$$

Denoting the distance from the Rowland circle to the source and the photographic film by $c$ and $g$, respectively, we obtain the linear magnification in the meridional plane:

$$V=\frac{g}{c}=\frac{R[a-\sin\ \theta(2a\ \sin\ \theta-R)}{(R\ \sin\ \theta-a)}(2a\ \sin\ \theta-R). \tag{10}$$

Analysis of Eqs. (9) and (10) shows that an anamorphic image is formed in this scheme (i.e., an image with differing

sagittal and meridional magnification). Within a certain range of distances from an object to the vertex of the crystal, the anamorphic factor is $K=G/V=0.3$–3. In this case, images can be obtained at any wavelength in the range $\sqrt{2}d/n<\lambda<2d/n$. If the distance from the object to the vertex of the crystal equals twice the sagittal focal length ($a=R/\sin\theta$), the magnifications are the same, and equal to unity:

$$G=V=1.$$

Spatial resolution in the meridional and sagittal planes is affected by various physical factors. In the sagittal plane, it is determined by aberrations of the spherical surface, while in the meridional plane, the resolution is also affected both by the nonmonochromatic nature of the source and the width of the rocking curve of the crystal. We attempted to estimate experimentally the spatial resolution using the x-ray emission from a laser plasma.[12] To do so, we focused the image of a test object illuminated by the plasma on the film, rather than the image of the laser "plume" itself. The test object consisted of two metallic grids superimposed on one another. Our results are shown in Fig. 4. The spatial resolution was better than 100 $\mu$m in both directions, with a field of view of at least 15 mm.

We managed to use the FSPR-2 scheme to investigate the radiative properties of various plasma objects; results are given in Sec. 4.

*2.1.3.3. X-ray microscope.* One type of FSPR-2 scheme that is useful when the angle $\theta$ is close to normal is the so-called x-ray microscope (see Fig. 5b), which can be used to obtain a monochromatic image of a plasma with high magnification and good spatial resolution that is essentially the same in both the meridional and the sagittal planes (see, e.g., Refs. 1, 13). In this geometry, the spatial resolution is governed by aberrations of the spherical reflector and the quality of the crystal. This scheme can therefore be used to obtain spatial resolution down to 5 $\mu$m, which enables one to investigate the structure of the source in detail. Note, however, that an image can be constructed only at wavelengths near an integer submultiple of twice the interplanar distance (i.e., $\lambda=2d/n$), which imposes certain limitations on the use of this scheme; however, it ensures that the resulting image is highly monochromatic.

We now discuss the possibility of using monochromatic x-ray emission from a plasma to backlight plasma objects. The scheme (see Fig. 5c) is essentially identical to the x-ray microscope scheme described above. The difference is that here we are interested not in the structure of the x-ray source, but in the structure of the object backlit by x rays from the supplementary source (which can be any plasma system, i.e., a laser plasma or a $Z$- or $X$-pinch plasma). In this scheme, the source of x rays is also located near the optical axis of the crystal mirror, but on the Rowland circle. A shadowgram of the object under study, which is located in the path of the x rays between the source and the spherical crystal mirror at a distance $a$ from the mirror, is produced at a distance $b$ from the mirror; the lens formula gives $1/a+1/b=1/F$, where $F$ is the focal length of the mirror. The spatial resolution along the object does not depend on the size of the x ray source in this scheme, but is instead determined by aberrations of the spherical mirror and the selectivity properties of the crystal. The size of the x ray source 2 determines the spectral composition of the radiation producing the image of the object:

$$\Delta\lambda=r(\lambda/R)\cot\theta. \tag{11}$$

Because all radiation from the source is focused to a small spot near the Rowland circle, the photographic film can be effectively shielded from intrinsic radiation emitted by the object under investigation and from other sources by using, for example, a screen with an iris diaphragm.

We ran experimental checks[14] using the emission from an $X$ pinch produced by fine aluminum wires, and a 15×50 mm$^2$ spherical mica crystal with radius of curvature $R=186$ mm. A steel mesh with 0.04 mm spacing and fine Al wires of 37 and 15 $\mu$m diameter were used as test objects. To produce the plasma object, a portion of the current in a diode was passed through the aluminum wire.

The experimental results are presented in Figs. 6d and 6e, which show a shadowgraph of the grid, 15-$\mu$m Al wires, and the expanding plasma produced by the explosion of an Al wire of the same diameter. The crystal was tuned to the $1s^2-1s3p$ line of the [He]-like Al ion. The size of the x-ray source in the light of this line, which was monitored using the x-ray microscopy scheme with a spherical mica crystal with $R=250$ mm (see Fig. 6b), was about 1 mm (Fig. 6c). This is consistent with the spectral range of the imaging radiation, which was approximately 0.002 Å. The spatial resolution obtained in these experiments was of order 15 $\mu$m over a 4×10 mm image field. Spatial resolutions of better than 10 $\mu$m were also obtained in an experimental check

TABLE I. Comparison between x-ray lasers based on the Ta XLVI ion (Ref. 17), and monochromatic collimated x-ray beams obtained from an X-pinch plasma (Ref. 15) and from plasmas heated by picosecond Nd laser pulses (Ref. 16).

| X-ray source | Wave length, Å | Monochromaticity, $\Delta\lambda/\lambda$ | Beam size, mm | Energy, $\mu$J | Pulse duration, ns | Divergence, $10^{-4}$ rad |
|---|---|---|---|---|---|---|
| $X$-pinch | 9.87–9.94 | $4\cdot10^{-3}$ | 10 × 45 | 3.2 | 5–10 | 5 × 5 |
| Picosecond Nd-laser | 3.95–3.98 | $4\cdot10^{-3}$ | 10 × 45 | 2 | 2–5 | 5 × 5 |
| Ta XLVI x-ray laser | 9.22 | $3\cdot10^{-3}$ | 10 × 30 | 0.3 | 0.01–0.02 | 6 × 6 |
| | 45 | $10^{-4}$ | 0.075 × 0.05 | 10 | 0.2 | 100 × 200 |

using a mesh with a period of 100 $\mu$m and a wire diameter of 25 $\mu$m, similar to the foregoing (a $10\times30$ mm$^2$ spherical crystal of mica with $R=100$ mm was used). The x-ray backlight source was a plasma heated by a pulsed Nd laser with energy $\sim10$ J and pulse width 2 ns.

*2.1.3.4. Production of high-intensity monochromatic collimated beams of soft x rays.* Monochromatic collimated beams of soft x rays can be produced by positioning an x-ray source in the focal plane of the crystal mirror. In Fig. 5a we show an experimental layout designed to produce parallel monochromatic beams using a spherical crystal. Because reflection from the crystal is selective, the radiation that participates in creating the beam lies in a certain wavelength interval,

$$\Delta\lambda=2d(\sin\theta_{\max}-\sin\theta_{\min})/m, \tag{12}$$

where $\theta_{\max}$ and $\theta_{\min}$ are the maximum and minimum grazing angles at the crystal surface, which are determined by the mutual disposition of the mirror and source. Inasmuch as $\theta_{\max}=90°$, while $\theta_{\min}$ is determined by the crystal aperture, we can also write Eq. (12) in the form

$$\Delta\lambda=(2d/n)[1-\cos(D/4F)], \tag{13}$$

where $D$ and $F$ are the mirror diameter and focal length. The ultimate characteristics of the collimated beams (divergence, spatial uniformity) are determined by the size of the source, spherical aberrations of the mirror, width of the rocking curve of the crystal, and quality of the spherical mirror.

We performed experiments in which collimated monochromatic beams were obtained in the wavelength interval 4–10 Å using a high-quality mica crystal with $R=250$ mm in the light from an $X$ pinch produced by Pd and Cu wires.[15] The quality of the beams thus generated was monitored by positioning a pair of metallic grids at various distances from the photographic film. Figures 6a and 6b show densitograms and shadowgrams of the test objects—metallic grids superimposed on one another (the wire thicknesses were 15 and 40 $\mu$m spaced at 100 $\mu$m and 1.2 mm, respectively)—obtained by illumination with a collimated beam of x rays from the $X$ pinch (the grids were approximately 2 cm from the film). Measurements of the transverse dimensions of the wires in the shadowgrams of the test object yield a beam divergence of $5\cdot10^{-4}$ rad. The spectral composition of the beam was recorded using a spectrograph with a convex crystal of CsAP (see Sec. 2.1). In Table I we compare the characteristics of the beams obtained in these experiments, and also in experiments where a plasma is heated by a picosecond laser,[16] with x rays from a Ta laser[17] at a wavelength of $\lambda=45$ Å, which is at present one of the shortest-wavelength x-ray lasers available. From this table it is clear that certain characteristics of the beams obtained here (wavelength, divergence, size) are better than the same characteristics of the Ta laser.

## 2.2. Instruments with Fresnel and Bragg–Fresnel x-ray optics

We now consider a class of x-ray imaging spectrographs in which the dispersive and focusing elements are Fresnel and Bragg–Fresnel structures.[18,19]

### *2.2.1. Transmission diffraction gratings*

Crystal spectrographs can no longer operate in the spectral range from 30 to 100 Å . Therefore, in this range the basic spectroscopic instrument used in our experiments was a transmission diffraction grating. Despite the fact that their spectral resolution is coarser than that of crystal spectrographs and oblique-incidence spectrographs, gratings possess a number of advantages that make them a very valuable diagnostic instrument.

Transmission gratings have at least one imt advantage: they can be used to measure the absolute intensity of soft x rays. Calculating the transmission of a grating is relatively simple, an important factor being that the calibration curve is smooth in the 20–100 Å spectral range, especially for the tungsten grating that we actually used. Note that analogous calculations for crystal spectrographs yield results that are difficult to apply to quantitative estimates, because the sharp

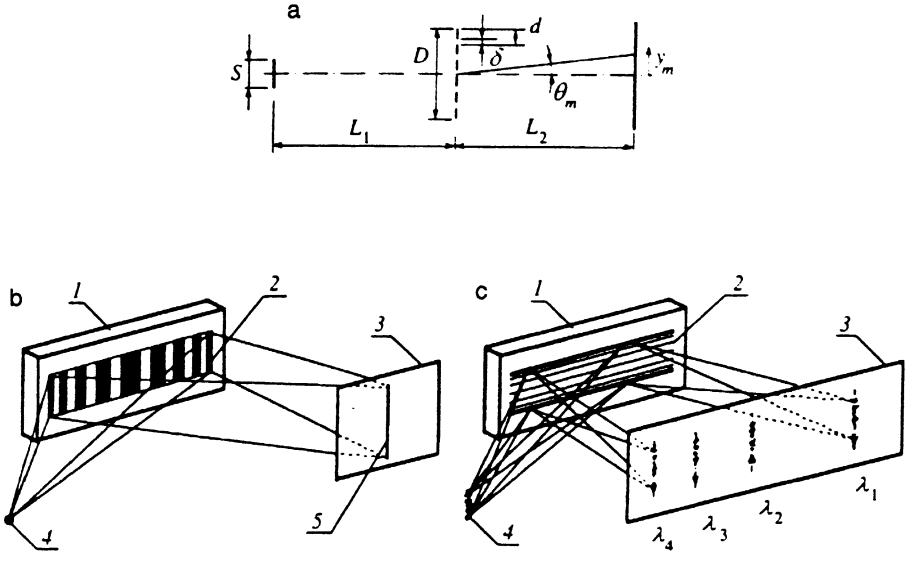


FIG. 7. Optical layout for Fresnel and Bragg–Fresnel dispersive structures: a) using a transmission diffraction grating to record the plasma emission; b) using a Bragg–Fresnel lens deposited on an artificial multilayer mirror oriented so as to focus in the direction of the dispersion; c) using a Bragg–Fresnel lens deposited on a crystal so as to focus in the direction perpendicular to the dispersion. *1*—crystal; *2*—Bragg–Fresnel structure; *3*—photographic film; *4*—source; *5*—image.

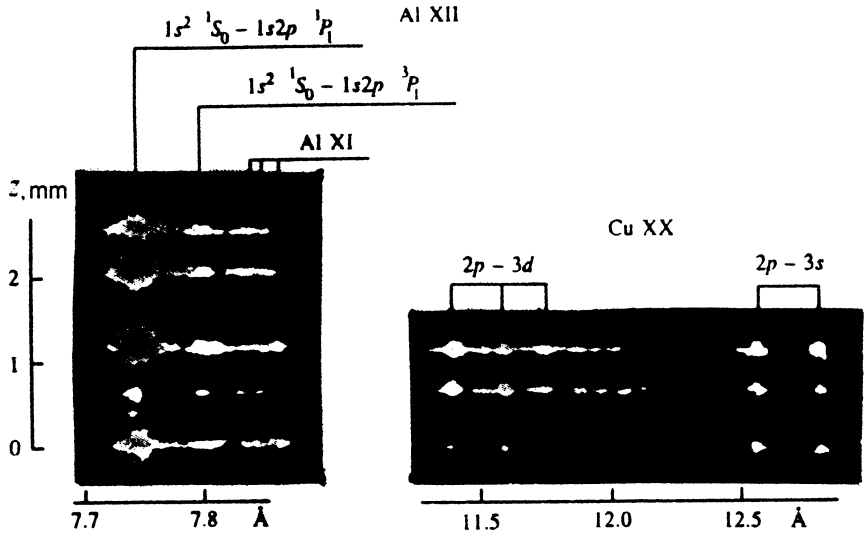


FIG. 8. Image of a Z-pinch plasma in the emission near a resonance line of the He-like Al XII ion, and in the Ne-like lines of the Ne-like Cu XX ion. Z is the distance in the cathode–anode direction. These images were obtained using a crystal with a deposited Fresnel structure.

jumps in the crystal reflection coefficient as a function of wavelength due to the $K$ and $L$ absorption edges of the elements in the crystal lead to considerable uncertainty in their interpretation.

In our experiments,[20,21] we used a tungsten pellicle 0.36 $\mu$m thick as a transmission grating. A 25 $\mu$m-diameter periodic structure was fashioned on the pellicle, consisting of free-standing (unsupported) stripes 1 $\mu$m apart, with a 1:1 strip-to-gap factor.

Figure 7a shows the layout of the grating experiments. $L_1$ and $L_2$ are distances from the object to the grating and from the grating to the recording film, respectively, $S$ and $D$ are the diameters of the source and aperture, and $d$ is the period of the grating. In order to shield from hard x rays, we positioned a 50-micron tantalum foil screen with a small opening (50–150 $\mu$m diameter) in front of the grating.

The dispersion of x rays in the plane of the film is determined by

$$Y_m = L_2 \sin \alpha_m = L_2 m\lambda/d, \tag{14}$$

where $m$ is the diffraction order, $Y_m$ is the distance in the direction of dispersion in the recording plane, $\alpha_m$ is the diffraction angle for the $m$th diffraction order, and $\lambda$ is the wavelength of the x rays. The limiting resolution in the ideal case is determined by the number $N$ of stripes in the grating aperture:

$$\Delta\lambda_d = \frac{\lambda}{mN}. \tag{15}$$

In practice, it is necessary to allow for blurring of the image due to the finite size of source and aperture:

$$\Delta Y = D\,\frac{L_1+L_2}{L_1} + S\,\frac{L_1}{L_2}. \tag{16}$$

From Eqs. (14) and (16), it follows that the spatial resolution $\Delta\lambda_s$ along the dispersion axis is

$$\Delta\lambda_s = \frac{d}{m}\left(\frac{S+D}{L_1} + \frac{D}{L_2}\right). \tag{17}$$

Finally, the shortest wavelength $\lambda_{\min}$ that can be reliably detected is limited by the spatial size of the zero-order maximum, and is close to $\Delta\lambda_s$.

Substituting typical experimental values into the expressions for the spatial resolution $S=100$ $\mu$m, $D=25$ $\mu$m, $d=25$ $\mu$m, $d=1$ $\mu$m, $L_1=L_2\simeq 50$ cm, we find that for the first diffraction order, $\Delta\lambda_d = 4\cdot 10^{-2}\,\lambda$ and $\Delta\lambda_s = 2.6$ Å.

Thus, it is clearly impossible to achieve diffraction-limited resolution at wavelengths $\lambda<65$ Å, and the quality of the spectrogram is determined by the physical dimensions of the source, aperture, etc. Nevertheless, the use of a grating is fully justified at $\lambda>65$ Å, where it operates with diffraction-limited resolution. Our use of gratings to investigate various pinch plasmas is detailed in Sec. 4.

#### 2.2.2. Use of multilayer Bragg–Fresnel lenses in x-ray imaging spectroscopy

Of the various elements used in Bragg–Fresnel x-ray optics, one group consists of elements with the topology of a zone plate based on a multilayer mirror or crystal.[8,10,22–24] Because these elements simultaneously have spectral selectivity and focusing properties, they can be used both to obtain focused images of a source in a spectral line and to record spectra over a wide spectral range with high spatial resolution.

The spatial resolution of a Bragg–Fresnel structure is determined by the width $\delta$ of the last zone, and depends on the diffraction order $m$. It follows from Ref. 18 that the distance $\rho_m$ between two points of an image that are resolvable in the radial direction is $\rho_m = 1.22\delta/m$. The resolution $\Delta f_m$ in the axial direction is related to $\rho_m$ by $\Delta f_m = 5.37\rho_m^2/\lambda$. The spatial resolution of a Bragg–Fresnel lens can be as small as a fraction of a micron.

To make spectroscopic measurements in our experiments, we employed two types of Bragg–Fresnel lenses (one based on a multilayer mirror, the other on a mica crystal), fabricated at the Institute for Problems in Microelectronics Technology of the Russian Academy of Sciences. For one of these, a linear Fresnel structure was made by etching through

TABLE II. Spectral lines of multiply charged aluminum ions.

| Ion | Transition | $\lambda_{theor}$, Å | | | | $\lambda_{exp}$, Å | | |
|---|---|---|---|---|---|---|---|---|
| | | A | B | C | D | E | F | G |
| Al XIII | $4p\ ^2P_{3/2,1/2}$–$1s\ ^2S_{1/2}$ | – | 5.73927 | – | – | 5.73927 | – | – |
| Al XII | $1s^1 2p\ ^1P_1$–$1s^2\ ^1S_0$ | 5.98272 | – | – | 5.98271 | – | 5.98278(50) | 5.98271(55) |
| Al XII | $1s11p\ ^1P_1$–$1s^2\ ^1S_0$ | 5.99019 | – | – | 5.99018 | – | 5.98981(50) | 5.99023(55) |
| Al XII | $1s10p\ ^1P_1$–$1s^2\ ^1S_0$ | 6.00003 | – | 6.00004 | 6.00003 | 6.00035(40) | 6.00035 | 6.00035 |
| Al XII | $1s9p\ ^1P_1$–$1s^2\ ^1S_0$ | 6.01340 | 6.01340 | 6.01340 | 6.01340 | 6.01314(40) | 6.01323(40) | 6.01340(40) |
| Al XII | $1s8p\ ^1P_1$–$1s^2\ ^1S_0$ | 6.03217 | 6.03219 | 6.03219 | 6.03218 | 6.03255(40) | 6.03255 | 6.03255 |
| Al XIII | $3p\ 2P_{3/2,1/2}$–$1s\ ^2S_{1/2}$ | – | 6.05291 | – | – | 6.05291 | – | 6.05282(40) |
| Al XII | $1s7p\ ^1P_1$–$1s^2\ ^1S_0$ | 6.05976 | 6.05976 | 6.05979 | 6.05978 | 6.06007(30) | 6.06007 | 6.06007 |
| Al XII | $1s6p\ ^1P_1$–$1s^2\ ^1S_0$ | 6.10276 | 6.10276 | 6.10282 | 6.10279 | – | 6.10281(40) | 6.10279(40) |

*Note.* A—Ref. 39; B—Ref. 44; C—Quantum defect method (Ref. 61); D—Quantum defect method using data from Ref. 44; E—Laser plasma experiment (spectrograph $R$=100 mm); F—Laser plasma experiment (spectrograph $R$=186 mm); G—$X$-pinch experiment (spectrograph $R$=100 mm).

141 layers of a W/Si multilayer mirror with a pattern spacing (i.e., the distance between alternate planes) of 64 Å. The lens aperture was 1×5.6 mm$^2$, the width of the outermost zone was 3.5 $\mu$m, the focal length was $f_0$=7 cm, and the mean Bragg angle was 1.34° for a wavelength of 1.5 Å . Since this structure, like any zone plate, has more than one diffraction order (theoretically an infinite number), in addition to the primary focus $f_0 = D\delta/\lambda$ (where $D$ is the diameter of the zone plate and $\delta$ is the size of the last zone) there are other foci $f_n = f_0/n$ as well, where $n$ is an odd integer. The intensity at a higher ($n$th) order focus is lower than the intensity of the primary focus by a factor of $n^2$, so the maximum attainable spatial resolution is $n$ times better. A sketch of the multilayer Fresnel mirror used in our experiments is shown in Fig. 7b.

Another type of Bragg–Fresnel lens used in these experiments consisted of a Fresnel structure in a copper layer sputtered onto the surface of a mica crystal ($2d$=19.94 Å). The thickness of the copper (0.25 $\mu$m) was chosen to ensure that x rays at the operating wavelength were phase shifted by $\pi$ upon reflection. The lens aperture was 1 cm×108.5 $\mu$m; for $\lambda$=7.75 Å, the focal length was 8 cm, and the width of the last zone, which determines the attainable spatial resolution, was 0.5 $\mu$m.

In contrast to the Bragg–Fresnel lens discussed above, which was based on a multilayer mirror, the copper-layer lens was positioned in such a way as to focus in the direction perpendicular to the dispersion direction (Fig. 7c). This experimental geometry enabled us to obtain a focused image of the source with high spatial resolution over a wide spectral range (in one direction the Bragg structure of the crystal acts as a spectral selector of x rays, while in the perpendicular direction the Fresnel structure provides spatial resolution). The focus condition is the same at all wavelengths in the working spectral range (i.e., wavelengths that can be reflected given a specific mutual disposition of the crystal and source), since the distance from the crystal to the image plane does not depend on $\lambda$. In principle, one can tune this lens to x rays of any wavelength (in which case the focal length $f_1$ varies as $\lambda_0/\lambda_1$), and also use higher-order foci as necessary.

Figure 8 shows typical images with one-dimensional spatial resolution of a $Z$-pinch Al plasma (near a resonance line of the He-like Al XI ion) and a $Z$-pinch Cu plasma (in the $2p-3d$ and $2p-3s$ lines of the Ne-like Cu XX ion). It is clear from Fig. 8 that Bragg–Fresnel lenses make it possible to obtain high spectroscopic and spatial resolution.

## 3. HIGH-PRECISION WAVELENGTH MEASUREMENT AND IDENTIFICATION OF X-RAY SPECTRAL LINES OF MULTIPLY CHARGED IONS

Spectrographs with spherically curved crystals based on the FSPR-1 scheme are extremely effective in the experimental atomic spectroscopy of multiply charged ions. As noted earlier, this scheme provides high speed combined with a narrow instrumental function, which makes it possible to record even comparatively low-intensity line spectra with high spectral resolution. The availability of one-dimensional spatial resolution also turns out to be very useful in several problems involving the spectroscopy of multiply charged ions (see Sec. 3.1.2.).

Over the last five years, we have pursued this type of investigation using FSPR-1 spectrographs.[7,10,25–39] In this chapter, we will therefore quote only a few of our most recent results to illustrate the use of these spectroscopic instruments in problems of atomic spectroscopy.

### 3.1. Wavelength measurements in spectral transitions of multiply charged ions

In various problems of atomic physics, a question that often arises is how accurately the positions of energy levels of multiply charged ions are known. In many cases both experimental and theoretical data are available, and as a rule there is no way to know which of these should be given preference from the standpoint of accurately determining the spectroscopic constants. The only exceptions are multiply charged H-like ions, for which calculations necessarily provide higher accuracy than experiment, and ions with many unfilled shells (more than three), for which the experimental data are more accurate than the results of even the most detailed theoretical calculations. In the remaining cases, the

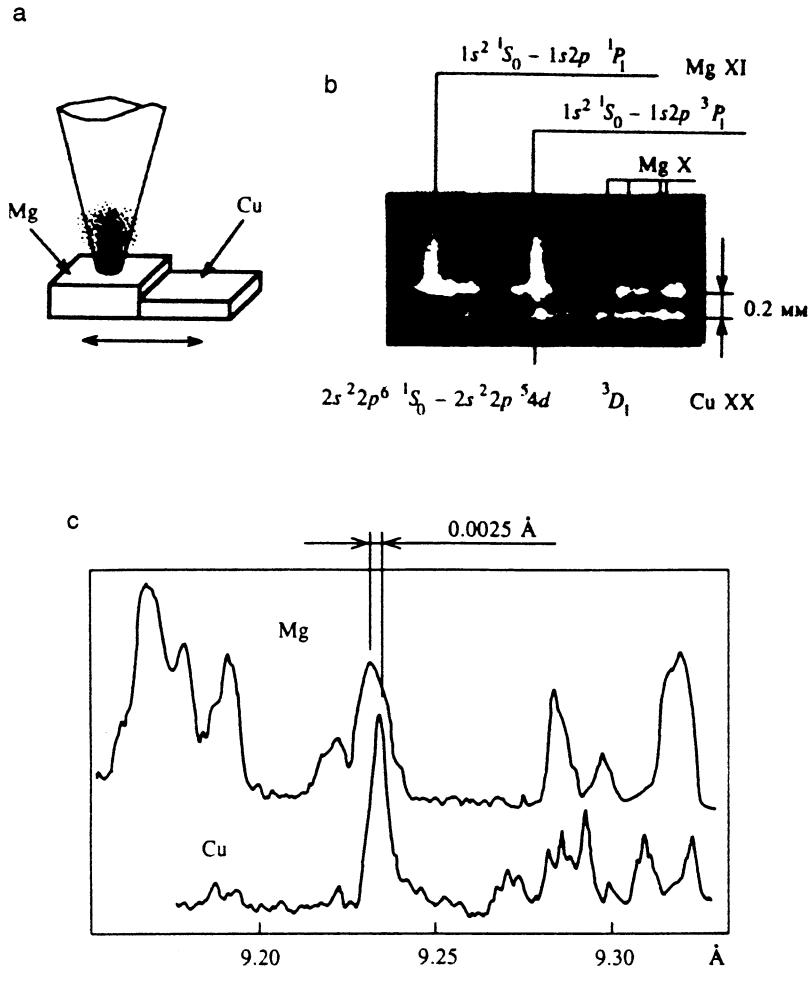


FIG. 9. a) Structure of targets used in experiments to measure the wavelength of closely spaced spectral lines of various ions; b, c) spectrogram and densitogram of the spectra near the He $\alpha$ resonance line of the Mg XI ion, and 2–4 transitions of the Ne-like Cu XX ion, obtained using an FSPR-1 spectrograph with a mica crystal with $R = 250$ mm. A Nd laser was used, with a pulse energy of order 20 J and a pulse duration of 2 ns.

problem of choosing one type of data over the other is far from trivial. This is so largely because it is impossible to assess the accuracy of theoretical calculations *a priori*, while a comparison of calculated results arrived at via different methods can yield only an indirect assessment of their merits. In these cases, high-precision absolute measurements of the wavelengths of spectral lines enable us, firstly, to obtain quantitative estimates of the accuracy to which the position of some energy level is known, and secondly, to assess the capabilities of various computational methods.

Note that for many problems in both applied and fundamental physics, it suffices in practice to know only relative, rather than absolute, values of the wavelengths of spectral transitions. Thus, for example, in designing a resonantly pumped x-ray laser, we require data not on the absolute wavelengths of the pumping and pumped spectral transitions, but only on their wavelength differences. Similarly, it is usually sufficient to know just the relative positions of spectral lines in order to decipher spectra and identify those lines. Although both relative and absolute wavelength measurements can be made using the same spectroscopic instruments, the former are somewhat simpler, since they do not require reference lines in the spectrum under investigation with wavelengths known to higher accuracy than that of the experimental results.

### 3.1.1. Absolute wavelength measurements of the resonance series for the He-like ion Al XII

The most accurate absolute measurements of the wavelengths of the first terms of resonance series of various mul-

TABLE III. Wavelength differences for resonance pairs.

| Resonance pair | $\Delta\lambda_{exp}$, Å | | |
|---|---|---|---|
| | Laser plasma | EBIT [29, 45] | PLT [29] |
| (a) | 0.0017 ± 0.0008<br>0.0016 ± 0.0009 | 0.0027 ± 0.001<br>0.0016 ± 0.0008 | 0.0031 ± 0.002 |
| (b) | 0.0025 ± 0.0008 | 0.0019 ± 0.0007 | |

*Note.* (a)—$2p\ ^2P_{3/2}$-$1s\ ^2S_{1/2}$ Mg XII and $2s2p^63p\ ^3P_1$-$2s^22p^6\ ^1S_0$ Ge XXIII: (b)—$1s2p\ ^3P_1$-$1s^2\ ^1S_0$ Mg XI and $2s^22p^54d\ ^3D_1$-$2s^22p^6\ ^1S_0$ Cu XX.

tiply charged He-like ions were made recently and described in Refs. 40 and 41. It was found that for transitions from levels with $n=2$, 3 (where $n$ is the principal quantum number), theory and experiment agreed to within $5\cdot10^{-5}$ Å in order of magnitude, which was within the limits of experimental error. However, high-precision measurement of the wavelengths of transitions from levels with $n\geqslant4$ constitutes a much more complicated experimental problem, by virtue of the low intensity of these spectral lines and their strong broadening in the plasma microfield. In steady-state plasma sources, the populations of highly excited states decrease rapidly with increasing $n$. For reliable detection of these lines, we therefore require a plasma with very high density. In such a plasma these lines are very broad, which increases wavelength-measurement errors. Of course, by reducing the plasma density we can reduce the width of these lines, but we rapidly reduce their intensities at the same time. Even in the best case, this also reduces measurement accuracy, while in the worst case it makes the transitions impossible to detect at all.

Accordingly, plasma sources traditionally used in the spectroscopy of multiply charged ions (vacuum sparks, tokamaks, dense laser plasmas, and, recently, EBIT) do not permit measurement of wavelengths of the higher components of the resonant series of He-like ions to accuracies comparable to those of theoretical calculations. The situation changes when a transient plasma is used, i.e., a recombining plasma where the dependence of level populations on $n$ has a considerably different character (usually nonmonotonic). In this case, emission spectra can be obtained in which the lines are both narrow (due to the lower plasma density) and an intense (due to the efficiency of the recombination channel for the populations of high-lying states). Such recombining plasmas can be obtained, for example, in the decay of micropinches or in the dispersal stage of a laser plasma. We have investigated these plasma sources as a way to study the higher ($n=6-12$) components of the resonance series for the He-like Al XII ion.[39]

Our experimental studies were carried out in two phases, at the P. N. Lebedev Institute of Physics of the Russian Academy of Sciences (Moscow), and the Institute for Plasma Physics and Laser Microsynthesis (Warsaw). In the first phase, we used the explosion of two aluminum wires in the X-pinch geometry to produce the plasma,[28] and in the second we used a Nd–glass laser[42,43] (6–15 J pulses 1 ns wide, on-target flux densities of $\sim10^{13}$ W/cm$^2$). In both cases, the x-ray emission of the plasma was recorded by FSPR-1 spectrographs with spherically curved mica crystals having radii $R_1=100$ mm and $R_2=186$ mm.

Figure 3a shows an example of the resulting spectrum, which contains higher terms of the $1snp\ ^1P_1-1s^2\ ^1S_0$ resonance series ($n=6-12$) of the He-like Al XII ion, and the $Ly_\beta$ and $Ly_\gamma$ lines of the H-like Al XIII ion. It is clear from this figure that plasma regions located near the point of production (i.e., the target surface for the laser plasma, or the point of intersection of the wires for the $X$ pinch) emit very broad spectral lines that are ill-suited to high-precision wavelength measurement. A fast spectrograph makes it possible to observe spectra of relatively tenuous plasma objects, however, which emit fairly narrow lines (about 3 mÅ), and to measure the wavelengths with relative errors $\Delta\lambda/\lambda\sim(5-8)\cdot10^{-5}$.

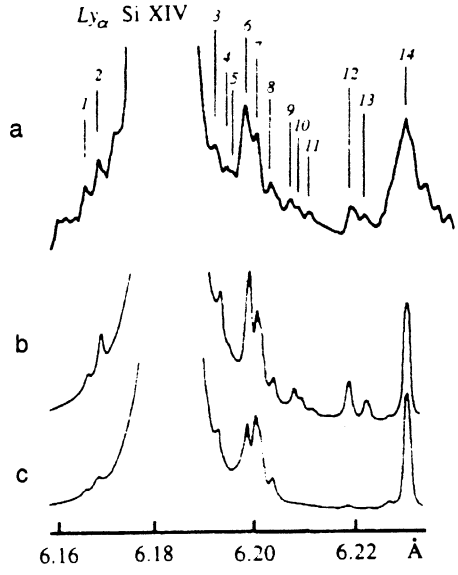


FIG. 10. a) Density of a segment of the spectrum obtained when a plasma is heated by x rays from a subpicosecond XeCl laser, in wavelength range 6.16–6.23 Å ; b) theoretical simulation of this segment of the spectrum given by radiative-collisional model with $N_e=6\cdot10^{22}$ cm$^{-3}$ and $T_e=460$ eV; c) the same segment of the spectrum as given by the corona model with $T_e=460$ eV.

We used the $Ly_\beta$ and $Ly_\gamma$ lines as primary references for wavelength measurements, as their wavelengths are known[44] to an accuracy of ±0.000007 Å, which is considerably better than the expected experimental errors (±0.0003–0.0005 Å). Table II lists the derived wavelengths and their measurement errors. It is clear from this table that the wavelength differences obtained in the various experiments are smaller than the estimated measurement accuracy. This may mean that the measurement errors are actually somewhat smaller (by 30–50%) than those shown in Table II.

In Table II, we also list the $1snp\ ^1P_1-1s^2\ ^1S_0$ transition wavelengths calculated by various methods (see Ref. 39 for details). It is clear that for transitions from highly excited levels, the differences between the theoretical and experimental values lie within the limits of experimental error.

#### *3.1.2. Measurement of wavelength differences for nearby spectral lines of different ions*

We remarked above that in certain problems, relative rather than absolute measurements of the wavelengths of x-ray spectral lines are of interest. One typical example of such a problem is the design of an x-ray laser with resonant photon pumping.[5] Our calculations show that these lasers can be more efficient than existing lasers based on recombination or collisional schemes when the wavelength difference between the strong pump line of one ion and the absorption line of the other (which is coupled to the upper level of the laser transition) is sufficiently small, i.e., at least smaller than the widths of these lines. Usually, however, one or both of the

TABLE IV. Satellite structure in the resonance line of the H-like Si XIV ion due to transitions of the type $2l3l'-1s3l'$.

| Line number | $\lambda_{exp}$, Å | $\lambda_{theor}$, Å | Transition |
|---|---|---|---|
| 1 | 6.1650 | 6.1644 | $2p3p\ ^1S_0-1s3p\ ^1P_1$ |
| 2 | 6.1677 | 6.1676 | $2p3d\ ^1P_1-1s3d\ ^1D_2$ |
| 3 | 6.1928 | 6.1928 | $2p3p\ ^1D_2-1s3p\ ^3P_2$ |
| | | 6.1928 | $2p3s\ ^3P_2-1s3s\ ^3S_1$ |
| 4 | 6.1948 | 6.1952 | $2p3s\ ^3P_1-1s3s\ ^3S_1$ |
| 5 | 6.1963 | 6.1974 | $2s3p\ ^3P_2-1s3s\ ^3S_1$ |
| | | 6.1963 | $2s3p\ ^3P_0-1s3s\ ^3S_1$ |
| 6 | 6.1986 | 6.1993 | $2p3d\ ^1D_2-1s3d\ ^1D_2$ |
| | | 6.1992 | $2p3d\ ^3F_4-1s3d\ ^3D_3$ |
| 7 | 6.2003 | 6.2019 | $2p3d\ ^3F_3-1s3d\ ^3D_2$ |
| | | 6.2015 | $2p3p\ ^1D_2-1s3p\ ^1P_1$ |
| | | 6.1991 | $2p^2\ ^1S_0-1s2p\ ^1P_1$ |
| 8 | 6.2039 | 6.2042 | $2p3d\ ^3F_2-1s3d\ ^3D_1$ |
| | | 6.2043 | $2p3d\ ^3F_2-1s3d\ ^3D_2$ |
| 9 | 6.2080 | 6.2078 | $2p3p\ ^3D_3-1s3p\ ^3P_2$ |
| 10 | 6.2095 | 6.2097 | $2p3p\ ^3D_2-1s3p\ ^3P_1$ |
| 11 | 6.2117 | 6.2119 | $2p3p\ ^3D_1-1s3p\ ^3P_0$ |
| 12 | 6.2186 | 6.2165 | $2p3p\ ^1P_1-1s3p\ ^1P_1$ |
| 13 | 6.2221 | 6.2238 | $2s3p\ ^1P_1-1s3s\ ^1S_0$ |

ions involved in the laser scheme are multielectron (Ne-like, for example), and existing theoretical methods are not accurate enough to calculate the wavelengths of their spectral lines. Therefore, only a high-precision experiment can definitively evaluate the feasibility of particular x-ray laser schemes based on resonant pumping.

We used an FSPR-1 spectrograph to assess the feasibility of two schemes for photon-pumped lasers,[28,29] in which the resonance doublet of the H-like Mg ion or the intercombination line of the He-like Mg ion are used as pump lines, while the absorption lines are the $2p-4d$ and $2s-3p$ transitions of the Ne-like Ge XXIII and Cu XX ions, respectively. In both cases, the experiments made use of a scheme resembling the one shown in Fig. 9. A characteristic feature of this scheme is the use of a stepped target, consisting of two plane targets of different materials (Mg and Ge or Cu and Mg), whose surfaces differ in height by 0.2–0.3 mm. Spectra were recorded in two laser bursts: first one part of the target was illuminated, then the target was shifted horizontally and the second burst produced a plasma of the other material. Since the FSPR-1 spectrograph provides one-dimensional spatial resolution in the vertical direction, by using this stepped target we were able, first of all, to spatially separate the emission spectra of the various elements recorded on the film, and secondly, we could measure the relative positions of the spectral lines of interest to us in those regions of the plasma where they are narrowest. This provided measurement accuracy of the resonance defect of a subject pair of lines to better than ±0.0008 Å (these results are listed in the column headed "Laser Plasma" in Table III). Note that although we were interested solely in relative measurements in these experiments, we actually measured the absolute wavelength of the $2s2p^63p\ ^3P_1-2s^22p^6\ ^1S_0$ line of Ge XXIII, since to the given measurement accuracy, the $Ly_{\alpha 1}$ line of Mg XII could be treated as an absolute reference.

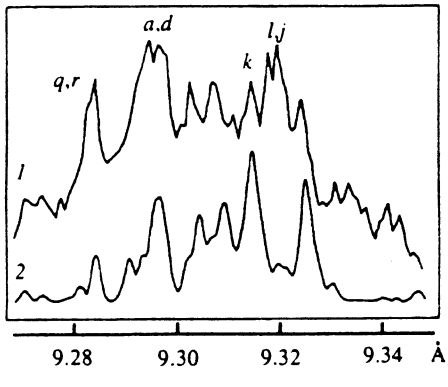


FIG. 11. 1) Density of a segment of the x-ray spectrum from a Mg plasma heated for 1 ns by light from a Nd laser (Refs. 26, 28). The traditional nomenclature $q, r, a, d, k, l, j$ is used for Li-like satellites (see, e.g., Ref. 1); 2) results of theoretical modeling of a spectrum consisting of $1s2p2l3l'-1s^22l3l'$ satellites of the Be-like Mg IX ion (with no Li-like satellites).

### 3.2. Identification of satellite structures in the *K*- and *L*-spectra of multiply charged ions

A characteristic feature of the emission spectra of multiply charged ions is the presence of lines resulting from radiative decay of doubly excited states. These lines, usually called dielectronic satellites (although not all of them are excited via dielectronic capture), are primarily observed as long-wavelength satellites of the corresponding resonance lines. Up to now, the most thoroughly investigated satellite structures have been those in the spectra of ions with a $K$-shell core (i.e., H- and He-like ions), with most of the available information pertaining to satellites of resonance lines that result from transitions in which the ion loses one unit of charge. Although there has always been great interest in investigating such structures (among other things, because these lines provide an exceedingly useful means of gauging plasma temperature and density), this interest has recently increased, if anything. There are a number of reasons for this: Plasmas obtainable in the laboratory contain more and more multiply charged ions, in whose emission spectra satellite structures begin to dominate resonance lines. The ionized state of a high-temperature plasma produced by picosecond and femtosecond laser pulses has distinctive features that lead to the emergence of many previously unobserved satellite structures in the x-ray spectra, due to transitions in ions of various isoelectronic sequences. The need for shorter and shorter-wavelength lasers based on transitions in multiply charged (Ne- and Ni-like) ions requires that satellite structures in $L$- and $M$-spectra that heretofore went essentially unstudied now be investigated. Diagnostics for ultradense plasmas based on resonance line shape require investigation of how satellites contribute to the observed profiles.

With regard to the experimental design, the study of satellite structures is generally a more complicated problem than studies of resonance transitions, for example, since we are then dealing with dozens of spectral lines concentrated

within a narrow spectral range. The x-ray spectrometer employed should therefore, on the one hand, provide very high spectral resolution, and on the other, be fast enough to record satellite structures emitted even by low-density regions of the plasma. At present, when it comes to recording and identifying certain new classes of satellite structures in the $K$- and $L$-spectra of multiply charged ions, FSPR-1 spectrographs best satisfy these requirements.

#### 3.2.1. Satellite structures in the K-spectra of Si and Mg ions

We studied the spectrum of silicon ions near the $Ly_\alpha$ resonance line of the H-like Si XIII ion in a laser plasma heated by a femtosecond pulse from the Los Alamos Bright Source II XeCl excimer laser.[37,46] An example of the spectrum obtained with an FSPR-1 spectrograph is shown in Fig. 10a. We found that the observed spectrum contains a much greater number of intense lines than corresponding spectra previously obtained in experiments with an $X$ pinch[28] and in a laser plasma heated by 2-ns pulses from a Nd laser.[1] Several of the observed lines are known dielectronic satellites due to $2p2l-1s2l$ transitions in the He-like Si XIII ion. The remainder (1–13 in Fig. 10a), located in immediate proximity to the resonance, turn out to be due to radiative decay of the $2l3l'$ levels of this same ion.

These lines were identified by comparing experimental and theoretical values of the transition wavelengths and intensities. The wavelengths were measured with a relative accuracy of $\pm 0.0008$ Å; however, since we used the previously

TABLE V. The most intense resonance-line satellites of the He-like Mg XI ion due to radiative decay of $1s2l2l'3l''$ levels of the Be-like Mg IX ion.

| Wavelength, Å | | Transition | |
|---|---|---|---|
| Experiment | Theory [26, 28] | Lower level | Upper level |
| 9.2824 | 9.2840 | $1s^22s3d\ ^3D_3$ | $1s2s[^1S]2p[^2P]3d\ ^3P_2$ |
| 9.2922 | 9.2929 | $1s^22s3d\ ^1D_2$ | $1s2s[^3S]2p[^2P]3d\ ^1F_3$ |
| 9.2981 | 9.2978 | $1s^22p3d\ ^3D_3$ | $1s(2p2[^1D])[^2D]3d\ ^3P_2$ |
| 9.3025 | 9.3017 | $1s^22s3p\ ^3P_2$ | $1s2s[^3S]2p[^2P]3p\ ^3P_2$ |
| | 9.3020 | $1s^22s3p\ ^3P_1$ | $1s2s[^3S]2p[^2P]3p\ ^3P_1$ |
| | 9.3026 | $1s^22s3p\ ^3P_1$ | $1s2s[^3S]2p[^2P]3p\ ^3P_0$ |
| | 9.3029 | $1s^22p3d\ ^1D_2$ | $1s(2p2[^1D])[^2D]3d\ ^1D_2$ |
| | 9.3035 | $1s^22s3s\ ^3S_1$ | $1s2s[^3S]2p[^2P]3s\ ^3P_2$ |
| | 9.3036 | $1s^22s3p\ ^3P_2$ | $1s2s[^1S]2p[^2P]3p\ ^3S_1$ |
| | 9.3041 | $1s^22s3p\ ^1P_1$ | $1s2s[^3S]2p[^2P]3p\ ^1D_2$ |
| | 9.3043 | $1s^22p3d\ ^3F_2$ | $1s(2p2[^3P])[^2P]3d\ ^1P_1$ |
| | 9.3044 | $1s^22p3d\ ^3D_3$ | $1s(2p^2[^3P])[^2P]3d^3D_3$ |
| | 9.3044 | $1s^22s3s\ ^3S_1$ | $1s2s[^1S]2p[^2P]3s\ ^3P_1$ |
| 9.3068 | 9.3065 | $1s^22p3d\ ^1P_1$ | $1s(2p^2[^3P])[^2P]3d\ ^1D_2$ |
| | 9.3066 | $1s^22p3d\ ^1F_3$ | $1s(2p^2[^3P])[^2P]3d\ ^1F_3$ |
| 9.3080 | 9.3079 | $1s^22p3d\ ^3D_1$ | $1s(2p^2[^1D])[^2D]3d\ ^3F_2$ |
| | 9.3085 | $1s^22p3d\ ^3D_2$ | $1s(2p^2[^1D])[^2D]3d\ ^3F_3$ |
| | 9.3091 | $1s^22p3d\ ^3D_3$ | $1s(2p^2[^3P])[^2P]3d\ ^3F_4$ |
| | 9.3094 | $1s^22s3d\ ^1D_2$ | $1s2s[^1S]2p[^2P]3d\ ^1D_2$ |
| | 9.3097 | $1s^22p3d\ ^3P_2$ | $1s(2p^2[^3P])[^2P]3d\ ^3D_3$ |
| | 9.3098 | $1s^22p3s\ ^1P_1$ | $1s(2p^2[^3P])[^2P]3s\ ^1P_1$ |
| 9.3111 | 9.3106 | $1s^22p3s\ ^3P_2$ | $1s(2p^2[^3P])[^2P]3s\ ^3P_2$ |
| | 9.3112 | $1s^22p3d\ ^3F_2$ | $1s(2p^2[^1D])[^2D]3d\ ^1G_3$ |
| | 9.3115 | $1s^22p3d\ ^3P_2$ | $1s(2p^2[^1D])[^2D]3d\ ^3P_1$ |
| 9.3132 | 9.3135 | $1s^22p3p\ ^3P_2$ | $1s(2p^2[^3P])[^2P]3p\ ^3S_1$ |
| | 9.3137 | $1s^22p3p\ ^3P_2$ | $1s(2p^2[^1D])[^2D]3p\ ^3P_2$ |
| | 9.3137 | $1s^22p3d\ ^3F_4$ | $1s(2p^2[^1D])[^2D]3d\ ^1G_4$ |
| 9.3214 | 9.3211 | $1s^22p3p\ ^3D_3$ | $1s2s[^3S]2p[^2P]3d\ ^3F_4$ |
| | 9.3215 | $1s^22p3d\ ^3F_2$ | $1s(2p^2[^1D])[^2D]3d\ ^1F_3$ |
| 9.3240 | 9.3239 | $1s^22p3d\ ^1D_2$ | $1s(2p^2[^1D])[^2D]3d\ ^1F_3$ |
| | 9.3240 | $1s^22p3d\ ^3P_2$ | $1s(2p^2[^1D])[^2D]3d\ ^3D_3$ |
| | 9.3247 | $1s^22p3p\ ^3D_2$ | $1s(2p^2[^3P])[^2P]3p\ ^3D_2$ |
| | 9.3249 | $1s^22p3p\ ^3D_1$ | $1s(2p^2[^3P])[^2P]3p\ ^3D_1$ |
| | 9.3251 | $1s^22p3p\ ^3D_3$ | $1s(2p^2[^3P])[^2P]3p\ ^3D_3$ |
| | 9.3252 | $1s^22s3p\ ^1P_1$ | $1s2s[^1S]2p[^2P]3p\ ^1P_1$ |
| | 9.3252 | $1s^22p3s\ ^3P_2$ | $1s(2p^2[^1D])[^2D]3s\ ^3D_3$ |
| | 9.3253 | $1s^22p3p\ ^3S_1$ | $1s(2p^2[^3P])[^2P]3p\ ^3P_2$ |
| 9.3265 | 9.3270 | $1s^22p3p\ ^3P_2$ | $1s(2p^2[^1D])[^2D]3p\ ^3D_3$ |
| 9.3282 | 9.3281 | $1s^22p3p\ ^1P_1$ | $1s(2p^2[^3P])[^2P]3p\ ^1S_0$ |
| 9.3308 | 9.3297 | $1s^22p3p\ ^1S_0$ | $1s(2p^2[^3P])[^2P]3p\ ^1P_1$ |
| | 9.3303 | $1s^22p3s\ ^1P_1$ | $1s(2p^2[^1D])[^2D]3s\ ^1D_2$ |
| 9.3333 | 9.3326 | $1s^22p3s\ ^1P_1$ | $1s(2p^2[^3P])[^2P]3s\ ^3P_2$ |

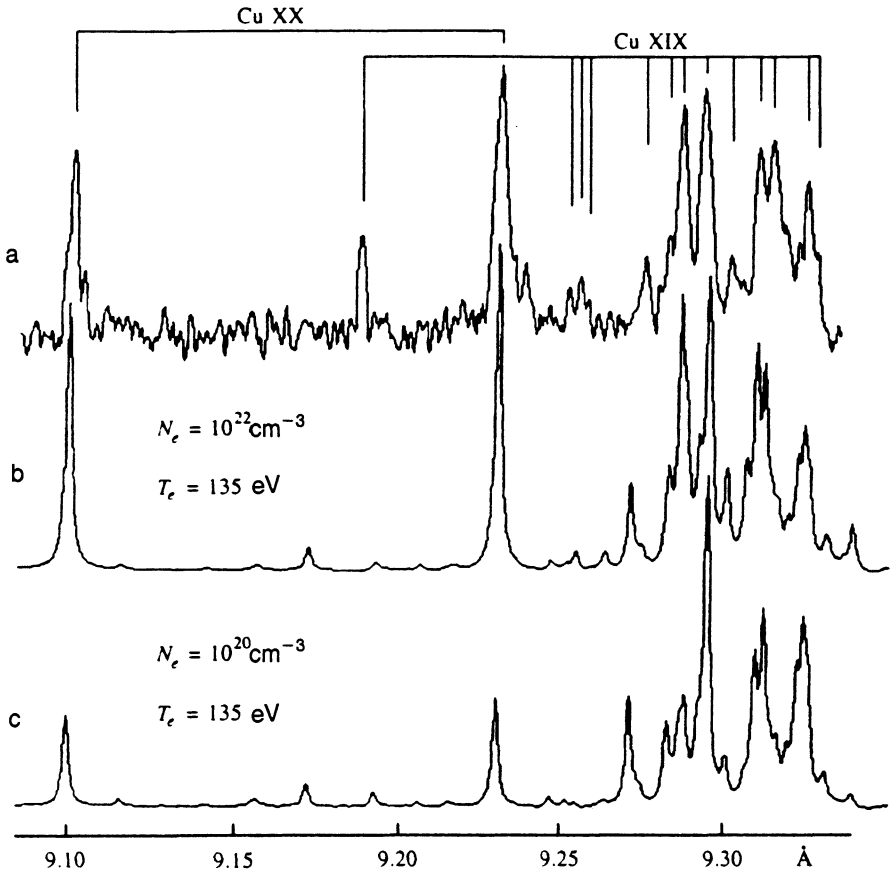


FIG. 12. a) Density of a segment of the x-ray spectrum near the $2s^22p^6\ {}^1S_0-2s^22p^54d\ {}^3D_1$, ${}^1D_1$ resonance lines of the Ne-like Cu XX ion (Ref. 33). Also shown here are satellite structures of the Na-like Cu XIX ion. b) Simulation of the experimental spectrum (A. Osterheld, Lawrence Livermore Laboratory) for $N_e = 10^{22}$ cm$^{-3}$ and $T_e = 135$ eV; c) same, for $N_e = 10^{20}$ cm$^{-3}$ and $T_e = 135$ eV.

identified $2p^2\ {}^1D_2-1s2p\ {}^1P_1$ and $2s2p\ {}^1P_1-1s2s\ {}^1S_0$ satellites as a reference, the absolute accuracy was somewhat lower, coming to $\pm 0.0015$ Å. Theoretical data on the wavelengths and probabilities of the $2s3l-1s3l$ transitions, and on the autoionization constants for the $2l3l'$ levels, were taken from the calculations of Refs. 47 and 48. A comparison of the experimental and theoretical wavelengths shows that all of the observed lines (1–13) correspond to some $2p3l-1s3l$ transition. However, a comparison of the experimental intensities of these lines with the values of the factors $Q_d$, which determine their intensities in the coronal limit, yields differences that are too large. The explanation is that the coronal model becomes inapplicable for an ultradense plasma (which is exactly the situation when a target is heated by an ultrashort laser pulse), since collisional mixing of doubly excited states of Si XIII is more efficient than collisionless decay when $N_e \geqslant 10^{22}$ cm$^{-3}$. By calculating the kinetics of the satellites based on a full radiation–collision model (see Fig. 10b), we can completely reconcile the experimental and theoretical data and reliably classify the satellite struc-

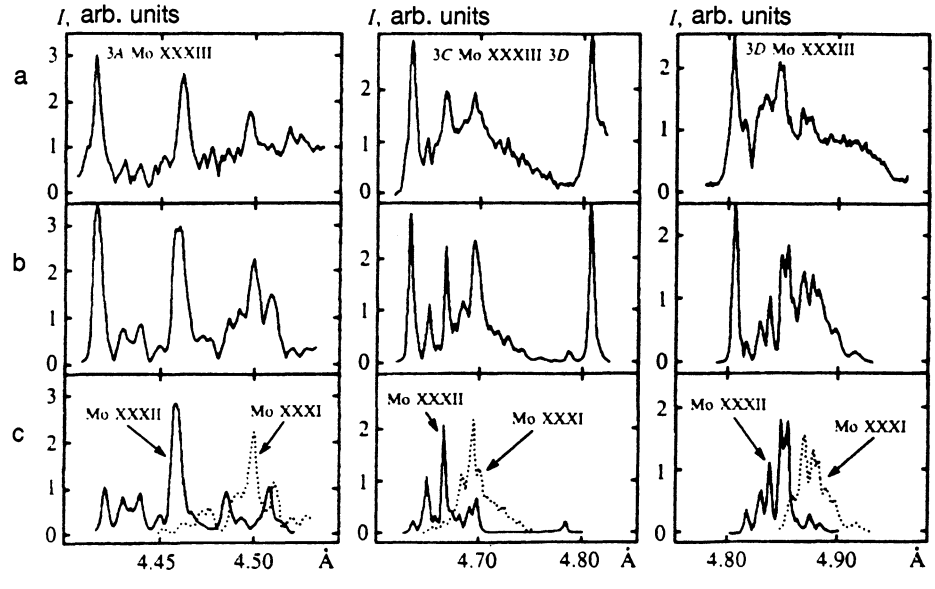


FIG. 13. a) Spectral density near the resonance lines (3A, 3C, 3D—see notation, e.g., in Ref. 1) for the 2–3 transitions of the Ne-like Mo XXXIII ion. b) The same segments of the spectra simulated while taking into account satellite structures of Na- and Mg-like ions; c) calculated results for the contribution from satellite structures of the Na- and Mg-like Mo XXXII and Mo XXXI ions.

TABLE VI. Na-like satellites (Ref. 13) of the $4d$-$2p$ lines of the Ne-like Cu XX ion.

| $\lambda_{exp}$, Å | $\lambda_{theor}$, Å | Transition | |
|---|---|---|---|
| 9.0984 | 9.0984 | $\left[\overline{2p}_{1/2}4d_{3/2}\right]_1$ | $-2s^22p^6$ |
| 9.1895 | 9.1924 | $\left[\overline{2p}_{3/2}3d_{3/2}4f_{5/2}\right]_{5/2}$ | $-3p_{3/2}$ |
| 9.2343 | 9.2340 | $\left[\overline{2p}_{3/2}4d_{5/2}\right]_1$ | $-2s^22p^6$ |
| 9.2547 | 9.2542 | $\left[\overline{2p}_{1/2}3d_{3/2}4d_{3/2}\right]_{3/2}$ | $-3d_{3/2}$ |
| 9.2760 | 9.2742 | $\left[\overline{2p}_{3/2}3p_{3/2}4p_{1/2}\right]_{3/2}$ | $-3s_{1/2}$ |
| | 9.2747 | $\left[\overline{2p}_{1/2}3p_{3/2}4d_{3/2}\right]_{1/2}$ | $-3p_{1/2}$ |
| 9.2829 | 9.2825 | $\left[\overline{2p}_{1/2}3p_{3/2}4d_{3/2}\right]_{1/2}$ | $-3p_{3/2}$ |
| | 9.2828 | $\left[\overline{2p}_{3/2}3d_{3/2}4p_{1/2}\right]_{1/2}$ | $-3p_{3/2}$ |
| | 9.2847 | $\left[\overline{2p}_{1/2}3p_{3/2}4d_{3/2}\right]_{3/2}$ | $-3p_{1/2}$ |
| 9.2873 | 9.2862 | $\left[\overline{2p}_{1/2}3s_{1/2}4d_{3/2}\right]_{1/2}$ | $-3s_{1/2}$ |
| | 9.2863 | $\left[\overline{2p}_{1/2}3s_{1/2}4d_{3/2}\right]_{3/2}$ | $-3s_{1/2}$ |
| | 9.2880 | $\left[\overline{2p}_{3/2}3p_{3/2}4p_{3/2}\right]_{3/2}$ | $-3s_{1/2}$ |
| 9.2933 | 9.2919 | $\left[\overline{2p}_{1/2}3p_{3/2}4d_{3/2}\right]_{3/2}$ | $-3p_{3/2}$ |
| | 9.2946 | $\left[\overline{2p}_{1/2}3p_{3/2}4d_{3/2}\right]_{5/2}$ | $-3p_{3/2}$ |
| | 9.2955 | $\left[\overline{2p}_{1/2}3p_{3/2}4d_{5/2}\right]_{3/2}$ | $-3p_{3/2}$ |
| 9.2999 | 9.3022 | $\left[\overline{2p}_{1/2}3p_{1/2}4d_{3/2}\right]_{1/2}$ | $-3p_{1/2}$ |
| 9.3089 | 9.3062 | $\left[\overline{2p}_{1/2}3d_{5/2}4d_{3/2}\right]_{3/2}$ | $-3d_{5/2}$ |
| | 9.3092 | $\left[\overline{2p}_{1/2}3d_{5/2}4d_{3/2}\right]_{5/2}$ | $-3d_{3/2}$ |
| | 9.3097 | $\left[\overline{2p}_{1/2}3d_{5/2}4d_{3/2}\right]_{7/2}$ | $-3d_{5/2}$ |
| 9.3126 | 9.3105 | $\left[\overline{2p}_{1/2}3d_{3/2}4d_{3/2}\right]_{1/2}$ | $-3d_{3/2}$ |
| | 9.3108 | $\left[\overline{2p}_{1/2}3p_{1/2}4d_{3/2}\right]_{3/2}$ | $-3p_{1/2}$ |
| | 9.3136 | $\left[\overline{2p}_{1/2}3s_{1/2}4d_{3/2}\right]_{3/2}$ | $-3s_{1/2}$ |
| 9.3164 | 9.3154 | $\left[\overline{2p}_{1/2}3d_{5/2}4d_{3/2}\right]_{3/2}$ | $-3d_{5/2}$ |
| | 9.3159 | $\left[\overline{2p}_{1/2}3p_{3/2}4d_{3/2}\right]_{3/2}$ | $-3p_{3/2}$ |
| 9.3202 | 9.3207 | $\left[\overline{2p}_{1/2}3d_{5/2}4d_{5/2}\right]_{7/2}$ | $-3d_{5/2}$ |
| 9.3236 | 9.3237 | $\left[\overline{2p}_{1/2}3d_{5/2}4d_{3/2}\right]_{5/2}$ | $-3d_{5/2}$ |
| 9.3257 | 9.3252 | $\left[\overline{2p}_{1/2}3d_{3/2}4d_{3/2}\right]_{5/2}$ | $-3d_{3/2}$ |

tures under study. Our results for the $2p3l-1s3l$ transitions are shown in Table IV.

Similarly, we have managed to decipher another type of satellite structure in the $K$ spectrum of magnesium detected in experiments where magnesium targets were heated by a picosecond laser pulse[25,26,28] (Max Born Institute, Berlin). In this case, we recorded previously unobserved spectral lines in the vicinity of the $1s2p\ ^1P_1-1s^2\ ^1S_0$ resonance line of the He-like Mg XI ion, which is located in the immediate neighborhood of known dielectronic satellites due to the $1s2l2l'-1s^22l'$ transitions of Li-like Mg X (see Fig. 11). We assumed that these lines were associated with radiative decay of the doubly excited $1s2l2l'3l''$ states of Be-like Mg IX. Calculations of the atomic constants and kinetics of Mg IX[26,28] confirm this assumption. In Fig. 11 we show those segments of the spectrum that contain the most intense satellites of this kind, obtained with an FSPR-1 spectrograph, along with the results of theoretical modeling, while in Table V we identify the most intense $1s2p2l3l'-1s^22l3l'$ satellites.

It is worth noting that the satellites we have identified have apparently been observed previously in strongly underionized laser plasmas, but inadequate spectral resolution precluded distinguishing them from the set of familiar Li-like satellites $q$, $r$, $a$–$d$, and $k$–$j$ (see Fig. 11), leading to difficulties in interpreting the intensities of the latter (see, e.g., Ref. 1).

### 3.2.2. Satellite structures in the L spectra of heavy ions

An example of satellite structure in the spectra of $L$ ions (i.e., ions with an $L$-shell core) is provided by the satellites of the resonance lines of Ne-like ions; the latter result from transitions of Na- and Mg-like ions. On the one hand, this situation is one of the simplest involving $L$ satellites to describe theoretically (because of closed or almost closed shells in the configurations of excited levels for both the Ne-like ion itself and the doubly excited states of the ions responsible for the satellite structure); on the other hand, these Ne-like ions may themselves be useful, a possibility of great interest for various applications.

We investigated satellite structures over the past few years for a number of heavy elements from Co to Mo, at first using spectrographs with crystals bent into cylindrical surfaces (Johann spectrographs), and later using FSPR-1 spectrographs. The use of the FSPR-1 spectrograph turns out to be of fundamental importance when the source of the spectrum is low-energy (in particular, when the plasma is heated by ultrashort or low-power laser pulses). Thus, for example, using the FSPR-1 we were able to detect satellites of the $n=4\rightarrow n'=2$ transition of Ne-like Cu XX in plasmas produced by a long pulse from a XeCl excimer laser at a flux density of order $10^{12}$ W/cm$^2$ (for laser pulse energies of $\simeq 4$ J and pulse durations of $\simeq 120$ ns). These experiments[33] were carried out at the Frascati Center of ENEA. An example of a spectrogram, along with the corresponding densitogram, is shown in Fig. 12, together with the results of theoretical modeling.[33] By comparing the theoretical and experimental data, we were able to identify a large fraction of the observed spectral lines as transitions from doubly excited levels of the Na-like Cu XIX ion (see Table VI and Fig. 12).

In investigating Na-like satellites, we used ion structure calculations based on the multiconfiguration Dirac-Fock method as implemented in the YODA and HULLAC programs (see, e.g., Refs. 35,49–51). The good agreement between calculated data and measurements shows that modern methods based on the theory of atomic spectra do indeed enable us to calculate the energy structure of multielectron ions with spectroscopic accuracy even for such complex objects as a Na-like ion with a vacancy in its $L$-shell. Therefore, we have recently attempted to use these methods to decipher still more complicated satellite structure in the resonance line of Ne-like ions due to radiative transitions from doubly excited $1s^22l^73l'3l''3l'''$ states of Mg-like ions.[35] These experiments were carried out at the XP laboratory at Cornell University; the plasma was generated by exploding two intersecting molybdenum wires ($X$-pinch geometry), and its x-ray spectrum was recorded in the 4.4–4.95 Å range by an FSPR-1 spectrograph.

Figures 13a–13c show sample densitograms of the spectra, together with the results of theoretical simulations that take Na- and Mg-like satellite structures into account. Table VII[21] lists the wavelengths of the Mg-like satellites we have

identified. From these figures it is clear that the Mg-like satellites are somewhat longer-wavelength than the Na-like satellites, as a rule. This implies that most of the observed spectral peaks are produced by radiative transitions of an ion of one isoelectronic sequence. However, in several cases (e.g., the lines at 4.463 Å, 4.509 Å, and 4.886 Å), they are a superposition of Na- and Mg-like satellites. In these instances, the experimental measurements yield some mean wavelength, which depends heavily on the relative abundance in the plasma of ions with various charge states, and which can differ when plasma sources of a different ionization state are used.

## 4. HIGH-TEMPERATURE PLASMA DIAGNOSTICS: X-RAY SPECTROGRAPHS WITH SPHERICALLY CURVED CRYSTALS

The x-ray techniques discussed in Sec. 2 can be used not only in the spectroscopy of multiply charged ions, as shown above, but also to extract information about the parameters of a plasma and the physical processes taking place within it. In this case, the advantages of the FSPR spectrograph, e.g., its high spatial resolution (in one or two dimensions) and speed, are most important, although high spectral resolution is still of no mean import, since many diagnostic methods are

TABLE VII. Wavelength of Mg-like resonance-line satellites of the Ne-like Mo XXXIII ion.

| $\lambda_{exp}$, Å | $\lambda_{theor}$, Å | Transition | | |
|---|---|---|---|---|
| | | upper level | lower level | $J_1$–$J_0$ |
| 4.473 | 4.4710 | $2s2p^6 3s_{1/2}3p_{3/2}3d_{5/2}$ | $3s_{1/2}3d_{5/2}$ | 2–2 |
| | 4.4737 | $2s2p^6 3s_{1/2}3p_{3/2}3d_{3/2}$ | $3s_{1/2}3d_{5/2}$ | 1–2 |
| | 4.4747 | $2s2p^6 3p_{3/2}3d_{5/2}3d_{5/2}$ | $3d_{3/2}3d_{5/2}$ | 3–4 |
| 4.477 | 4.4777 | $2s2p^6 3s_{1/2}3s_{1/2}3p_{3/2}$ | $3s_{1/2}3s_{1/2}$ | 1–0 |
| | 4.4751 | $2s2p^6 3s_{1/2}3p_{3/2}3p_{3/2}$ | $3s_{1/2}3p_{3/2}$ | 1–1 |
| | 4.4790 | $2s2p^6 3s_{1/2}3p_{3/2}3p_{3/2}$ | $3s_{1/2}3p_{3/2}$ | 2–2 |
| 4.491 | 4.4873 | $2s2p^6 3p_{3/2}3d_{5/2}3d_{5/2}$ | $3d_{5/2}3d_{5/2}$ | 4–4 |
| | 4.4878 | $2s2p^6 3s_{1/2}3p_{3/2}3d_{5/2}$ | $3s_{1/2}3d_{5/2}$ | 3–3 |
| | 4.4878 | $2s2p^6 3p_{3/2}3p_{3/2}3d_{5/2}$ | $3p_{3/2}3d_{5/2}$ | 4–4 |
| | 4.4926 | $2s2p^6 3p_{3/2}3p_{3/2}3d_{3/2}$ | $3p_{3/2}3d_{3/2}$ | 2–3 |
| 4.497 | 4.4994 | $2s2p^6 3s_{1/2}3p_{3/2}3d_{5/2}$ | $3s_{1/2}3d_{5/2}$ | 4–3 |
| | 4.5014 | $2s2p^6 3p_{3/2}3p_{3/2}3d_{5/2}$ | $3p_{3/2}3d_{5/2}$ | 5–4 |
| | 4.5016 | $2s2p^6 3p_{3/2}3d_{3/2}3d_{5/2}$ | $3d_{3/2}3d_{5/2}$ | 5–4 |
| 4.509* | 4.5090 | $2s2p^6 3s_{1/2}3p_{3/2}3d_{3/2}$ | $3s_{1/2}3d_{5/2}$ | 3–2 |
| 4.681 | 4.6807 | $2s^2 2p_{1/2}2p^4_{3/2}3s_{1/2}3d_{3/2}3d_{5/2}$ | $3s_{1/2}3d_{5/2}$ | 4–3 |
| | 4.6818 | $2s^2 2p_{1/2}2p^4_{3/2}3p_{3/2}3d_{3/2}3d_{5/2}$ | $3p_{3/2}3d_{5/2}$ | 2–3 |
| 4.690 | 4.6902 | $2s^2 2p_{1/2}2p^4_{3/2}3p_{3/2}3d_{3/2}3d_{5/2}$ | $3p_{3/2}3d_{5/2}$ | 5–4 |
| 4.697 | 4.7000 | $2s^2 2p_{1/2}2p^4_{3/2}3d_{3/2}3d_{5/2}3d_{5/2}$ | $3d_{3/2}3d_{5/2}$ | 4–4 |
| 4.715 | 4.7150 | $2s^2 2p_{1/2}2p^4_{3/2}3p_{1/2}3d_{3/2}3d_{5/2}$ | $3p_{1/2}3d_{5/2}$ | 2–2 |
| | 4.7152 | $2s^2 2p_{1/2}2p^4_{3/2}3d_{3/2}3d_{5/2}3d_{5/2}$ | $3p_{3/2}3d_{5/2}$ | 3–3 |
| 4.723 | 4.7207 | $2s^2 2p_{1/2}2p^4_{3/2}3s_{1/2}3d_{5/2}3d_{5/2}$ | $3s_{1/2}3d_{5/2}$ | 4–3 |
| | 4.7221 | $2s^2 2p_{1/2}2p^4_{3/2}3d_{3/2}3d_{3/2}3d_{5/2}$ | $3d_{3/2}3d_{3/2}$ | 2–2 |
| | 4.7231 | $2s^2 2p_{1/2}2p^4_{3/2}3d_{3/2}3d_{5/2}3d_{5/2}$ | $3d_{3/2}3d_{5/2}$ | 2–2 |
| 4.724 | 4.7237 | $2s^2 2p_{1/2}2p^4_{3/2}3s_{1/2}3d_{3/2}3d_{5/2}$ | $3p_{3/2}3p_{3/2}$ | 3–2 |
| 4.731 | 4.7313 | $2s^2 2p_{1/2}2p^4_{3/2}3d_{3/2}3d_{3/2}3d_{5/2}$ | $3d_{3/2}3d_{5/2}$ | 2–2 |
| | 4.7324 | $2s^2 2p_{1/2}2p^4_{3/2}3d_{3/2}3d_{3/2}3d_{5/2}$ | $3d_{3/2}3d_{5/2}$ | 5–4 |
| | 4.7336 | $2s^2 2p_{1/2}2p^4_{3/2}3p_{1/2}3d_{5/2}3d_{5/2}$ | $3p_{3/2}3d_{3/2}$ | 4–3 |
| 4.738 | 4.7387 | $2s^2 2p_{1/2}2p^4_{3/2}3p_{1/2}3p_{1/2}3d_{5/2}$ | $3p_{1/2}3p_{3/2}$ | 3–2 |
| | 4.7400 | $2s^2 2p_{1/2}2p^4_{3/2}3p_{1/2}3p_{1/2}3d_{5/2}$ | $3p_{1/2}3p_{3/2}$ | 2–1 |
| | 4.7402 | $2s^2 2p_{1/2}2p^4_{3/2}3p_{1/2}3d_{3/2}3d_{3/2}$ | $3p_{1/2}3d_{3/2}$ | 3–2 |
| 4.858 | 4.8588 | $2s^2 2p^2_{1/2}2p^4_{3/2}3p_{3/2}3d_{3/2}3d_{3/2}$ | $3p_{3/2}3d_{5/2}$ | 2–3 |
| | 4.8598 | $2s^2 2p^2_{1/2}2p^3_{3/2}3p_{3/2}3d_{3/2}3d_{5/2}$ | $3p_{3/2}3d_{5/2}$ | 3–4 |
| 4.872 | 4.8713 | $2s^2 2p^2_{1/2}2p^3_{3/2}3d_{3/2}3d_{5/2}3d_{5/2}$ | $3d_{3/2}3d_{5/2}$ | 2–3 |
| | 4.8713 | $2s^2 2p^2_{1/2}2p^3_{3/2}3s_{1/2}3p_{3/2}3d_{5/2}$ | $3s_{1/2}3p_{3/2}$ | 2–3 |
| | 4.8713 | $2s^2 2p^2_{1/2}2p^3_{3/2}3d_{5/2}3d_{5/2}3d_{5/2}$ | $3d_{3/2}3d_{5/2}$ | 3–3 |
| | 4.8714 | $2s^2 2p^2_{1/2}2p^3_{3/2}3s_{1/2}3p_{3/2}3d_{5/2}$ | $3s_{1/2}3p_{3/2}$ | 3–2 |
| | 4.8731 | $2s^2 2p^2_{1/2}2p^3_{3/2}3p_{3/2}3d_{3/2}3d_{5/2}$ | $3p_{3/2}3d_{3/2}$ | 2–2 |

TABLE 7. (*Continued.*)

| $\lambda_{exp}$, Å | $\lambda_{theor}$, Å | Transition | | |
|---|---|---|---|---|
| | | upper level | lower level | $J_1$–$J_0$ |
| 4.877 | 4.8780 | $2s^22p_{1/2}^2 2p_{3/2}^3 3d_{3/2}3d_{5/2}3d_{5/2}$ | $3d_{5/2}3d_{5/2}$ | 3–2 |
| | 4.8789 | $2s^22p_{1/2}^2 2p_{3/2}^3 3p_{3/2}3d_{3/2}3d_{3/2}$ | $3p_{3/2}3d_{3/2}$ | 4–3 |
| | 4.8790 | $2s^22p_{1/2}^2 2p_{3/2}^3 3d_{3/2}3d_{5/2}3d_{5/2}$ | $3d_{3/2}3d_{5/2}$ | 2–2 |
| 4.882 | 4.8817 | $2s^22p_{1/2}^2 2p_{3/2}^3 3p_{1/2}3d_{3/2}3d_{3/2}$ | $3p_{1/2}3d_{3/2}$ | 3–2 |
| | 4.8828 | $2s^22p_{1/2}^2 2p_{3/2}^3 3p_{3/2}3d_{3/2}3d_{5/2}$ | $3p_{3/2}3d_{5/2}$ | 5–4 |
| | 4.8839 | $2s^22p_{1/2}^2 2p_{3/2}^3 3p_{3/2}3d_{5/2}3d_{5/2}$ | $3p_{3/2}3d_{3/2}$ | 3–3 |
| 4.886* | 4.8853 | $2s^22p_{1/2}^2 2p_{3/2}^3 3d_{3/2}3d_{5/2}3d_{5/2}$ | $3d_{5/2}3d_{5/2}$ | 5–4 |
| | 4.8856 | $2s^22p_{1/2}^2 2p_{3/2}^3 3p_{3/2}3d_{5/2}3d_{5/2}$ | $3d_{3/2}3d_{3/2}$ | 3–2 |
| | 4.8864 | $2s^22p_{1/2}^2 2p_{3/2}^3 3d_{5/2}3d_{5/2}3d_{5/2}$ | $3d_{5/2}3d_{5/2}$ | 4–4 |
| 4.894 | 4.8932 | $2s^22p_{1/2}^2 2p_{3/2}^3 3d_{3/2}3d_{5/2}3d_{5/2}$ | $3d_{3/2}3d_{5/2}$ | 3–3 |
| | 4.8934 | $2s^22p_{1/2}^2 2p_{3/2}^3 3p_{3/2}3d_{3/2}3d_{5/2}$ | $3p_{3/2}3d_{5/2}$ | 4–3 |
| 4.901 | 4.9018 | $2s^22p_{1/2}^2 2p_{3/2}^3 3d_{3/2}3d_{5/2}3d_{5/2}$ | $3d_{3/2}3d_{5/2}$ | 5–4 |
| 4.914 | 4.9138 | $2s^22p_{1/2}^2 2p_{3/2}^3 3s_{1/2}3p_{3/2}3d_{5/2}$ | $3s_{1/2}3p_{3/2}$ | 3–2 |
| | 4.9144 | $2s^22p_{1/2}^2 2p_{3/2}^3 3d_{5/2}3d_{5/2}3d_{5/2}$ | $3d_{5/2}3d_{5/2}$ | 2–2 |

*Blended with Na-like satellites.

based either on comparing the characteristics of closely spaced spectral lines or on the profile of an individual line. Their combination of all these qualities enables one to use FSPR spectrographs to investigate various spatial regions of the most diverse plasma objects (see, e.g., Refs. 12, 28, 31, 34, 42, and 52–55).

From the standpoint of diagnostic applications, the FSPR-2 design is very promising, providing two-dimensional spatial resolution as it does. However, we were unable to fully exploit its advantages in the case of nonstationary plasma generation, because we had no way to record x rays with the required high temporal resolution (better than 1 ns). However, the solution to the ill-posed problem of recovering the spatial distribution of luminosity from a time-integrated image is insoluble, even for axial or centrosymmetric objects. Therefore, in our studies we used FSPR-1 spectrographs to obtain basic quantitative information, while the two-dimensional scheme was used to extract estimates that were qualitative rather than quantitative, albeit still very important in many cases.

### 4.1. Diagnostics of an ultradense plasma

By an ultradense plasma we mean a plasma with density close to that of a solid, i.e., with $N_e \geqslant 10^{22}$ cm$^{-3}$. Such plasmas can be obtained under laboratory conditions, e.g., in laser compression of spherical targets, micropinches, or when a plane solid-state target is heated by ultrashort laser pulses (see, e.g., Refs. 28, 31, 34, 37, 52, and 53). The pa-

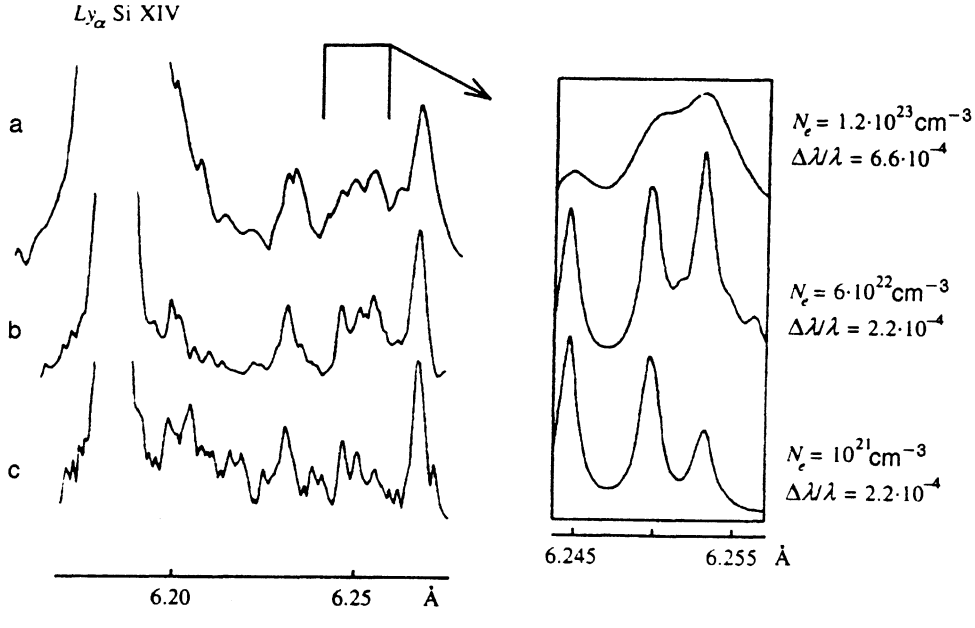


FIG. 14. Spectral density near the $Ly_\alpha$ line of the H-like Si XIV ion, recorded in the emission of various plasma sources: a) *X* pinch plasma (Ref. 28); b) plasma heated by 300-fs light pulses from a XeCl laser (Ref. 37); c) plasma heated by radiation from a Nd laser with 2-ns pulses (Ref. 1). Also shown in the figure are results of theoretical modeling of the satellite lines of Li-like Si XIII ions, corresponding to $2l2p^3P - 1s2l^3L$ transitions.

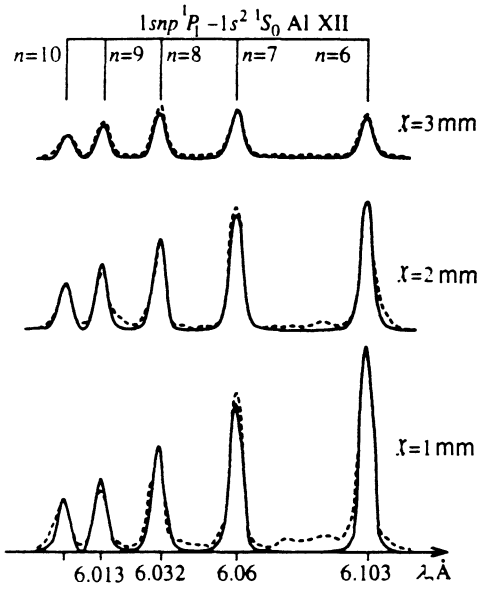


FIG. 15. Spectral density in an aluminum plasma (Refs. 42, 43) at various distances $X$ from the surface of the target over the wavelength range 6.0–1.11 Å . Dashed curves are experimental results, solid curves are the result of theoretical modeling.

rameters of these plasmas are ordinarily determined by x-ray spectroscopic methods based on comparing theoretical and experimental values of the intensities of $K$ satellites or resonance line profiles. Since ultradense plasma regions are normally small (no more than a few tens of microns), the x-ray spectroscopic technique used must possess at least this degree of spatial resolution; if this is not the case, averaging the luminosity over less dense regions of the plasma can significantly overestimate the parameters in the compressed zone. Generally speaking, the required spatial resolution can be obtained by using classical spectrographs with slit widths $\simeq$10–20 $\mu$m; however, because these instruments are slow, they cannot be used for diagnostics of low-energy ultradense plasma objects, e.g., plasmas produced by ultrashort laser pulses. For the FSPR-1 spectrograph there are no such limitations.

We used an FSPR-1 spectrograph to determine the parameters of an ultradense plasma at the hot spot of an $X$ pinch, and of plasmas heated by femto- and picosecond laser pulses. The diagnostic method we chose was the well-known method of determining plasma parameters from the relative intensities of dielectronic satellites of the resonance line of H-like ions (see, e.g., Refs. 28, 31, 34, 37, 52, and 53). These intensities are less sensitive to spatial averaging, since the intensity of the satellite structures falls off rapidly with distance from the hot region of a plasma, whereas resonance lines continue to radiate intensely at considerable distances due to repopulation of singly excited states of the ion in the course of recombination.

Figure 14 shows segments of spectra near the $Ly_\alpha$ resonance line of the H-like Si XIV ion obtained in experiments using (a) an $X$ pinch[28,52] and (b) a laser plasma produced by 300-fs pulses from a XeCl laser,[37] along with (c) the spectrum of a laser plasma heated by "long" ($\simeq$2 ns) pulses from a Nd laser.[1] In all three cases, the plasma density can be determined from the intensity ratio of the triplet satellites $2p^2\ ^3P-1s2p\ ^3P$ and $2s2p\ ^3P-1s2s\ ^3S_1$, which is sensitive to density. This technique yields $N_e=1.2\cdot10^{23}$, $6\cdot10^{22}$, and $10^{21}$ cm$^{-3}$ for experiments (a), (b), and (c), respectively. The high density in case (a) is also confirmed by observation of the forbidden satellite[56] $2p^2\ ^1D_2-1s2p\ ^3P_2$, while the density in case (b) is confirmed both by estimates of the width of the $Ly_\alpha$ resonance line for the Si XIV ion and by the relative intensities of satellites of type $2l3l'-1s3l'$.

Note that in case (b), the ratio of the intensities of the satellite $2p^2\ ^1D_2-1s2p\ ^1P_1$ and resonance lines yields the rather low value $T_e\simeq460$ eV for the electron temperature of the plasma. In this experiment, the flux density of the heating pulse is $q\simeq4\cdot10^{18}$ W/cm$^2$. Furthermore, before the primary laser pulse there is a pre-pulse that ensures the production of a pre-plasma. In light of these facts, the low value of $T_e$ and the value of the density $N_e=6\cdot10^{22}$ cm$^{-3}$, which exceeds the critical density for the heating x rays, imply that under the conditions of this experiment, the spatial region of the plasma where the luminosity peaks is located between the critical point and the surface of the solid.

For the $X$-pinch case, we investigated the explosion of wires made of glass and aluminum with various thicknesses. The temperature and density of the hot spots differed somewhat from one burst to the next, remaining in the range

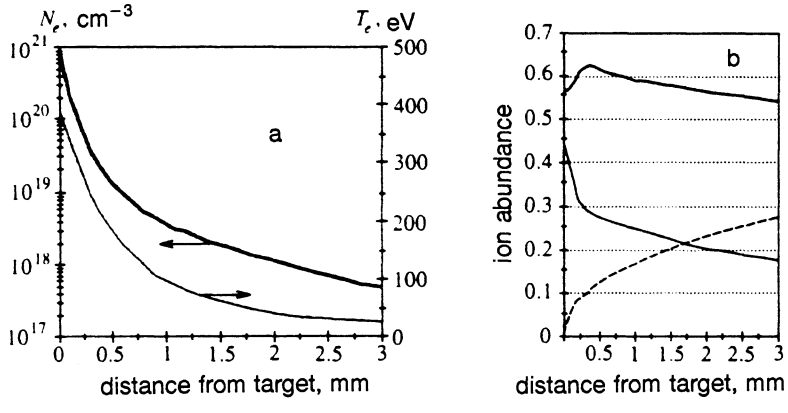


FIG. 16. a) Measured dependence of electron temperature and plasma density on distance to the target. b) Evolution of the ion content of an aluminum plasma as it expands over distances 0–3 mm (Refs. 42, 43). Lighter solid curve—H-like ions; heavier solid curve—He-like ions; dashed curve—sum of low-multiplicity ions.

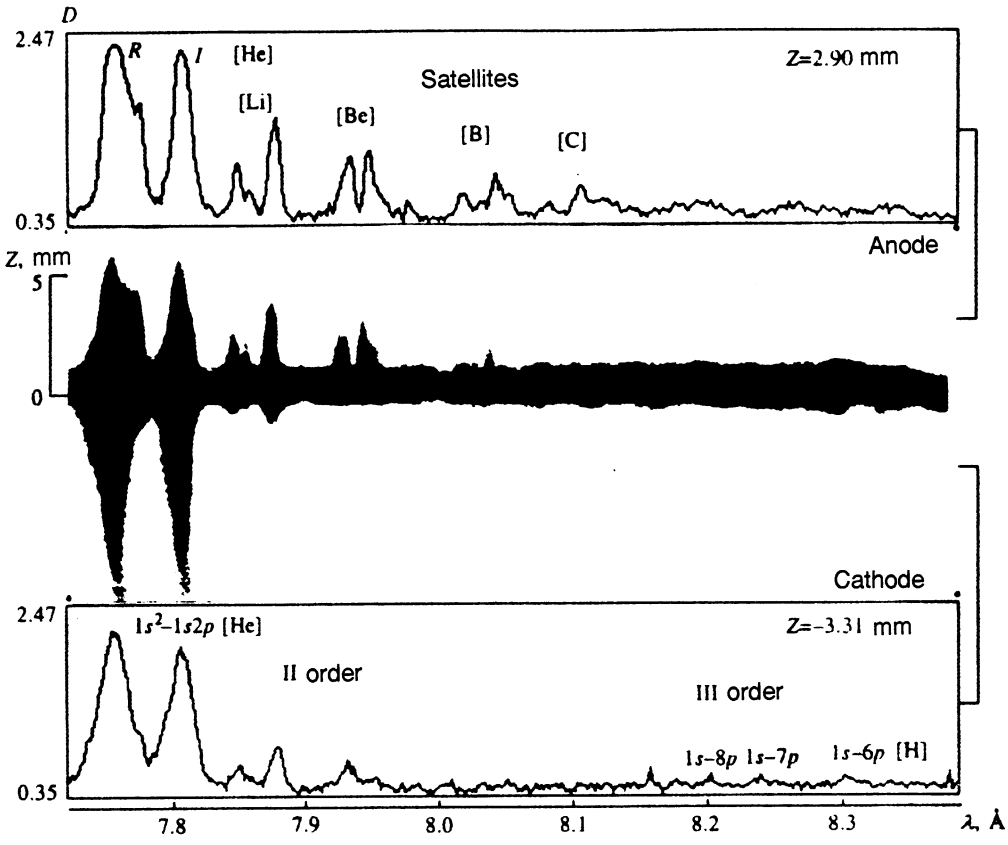


FIG. 17. Spectrogram and characteristic densitogram (in the directions of anode and cathode) near the $1s^2\,{}^1S_0-1s2p\,{}^1P_1$ resonance line of the He-like Al XII ion in experiments with an $X$ pinch (Ref. 59).

$N_e\sim10^{23}-10^{24}$ cm$^{-3}$ and $T_e=550-950$ eV, while the hot spot dimensions[28] never exceeded $\simeq30$ $\mu$m.

### 4.2. Diagnostics of pulse-generated plasma objects in their decay stage

Once the pulse that produces a high-temperature plasma has ended (or even somewhat sooner), its decay begins. At this stage, the density and temperature of the plasma fall, and its dimensions increase. X-ray spectroscopy makes it possible to follow the variations in plasma characteristics, and to track plasma evolution at this stage. At this point the most important requirement on the x-ray instrument is that it be fast: the faster the instrument, the fainter and less dense the plasma regions that can be studied. In this case, the requirements on spectral resolution are not very stringent, since usually only well-isolated spectral lines are observed (such as the resonance series of $K$ ions, for example).

In this section we illustrate the capabilities of FSPR spectrographs to address this kind of problem with two examples. The first of these is a study of a freely expanding laser plasma of aluminum[43] (for the conditions of this experiment see above, Sec. 3.1.1.). The use of fast FSPR-1 spectrographs enables us to obtain spectrograms suitable for quantitative processing, corresponding to distances from the target surface up to $x\simeq3-5$ mm. These spectrograms contain the $1snp\,{}^1P_1-1s^2\,{}^1S_0$ lines of the resonance series of He-like Al XII ions with $n=6-10$, whose intensity ratios are used to determine the plasma parameters. For this, we calculated the kinetics of the Al XII ion in plasma in the quasi-steady-state radiation–collision model for various values of $N_e$ and $T_e$. We then chose $N_e$ and $T_e$ for each distance $x$ so as to ensure agreement of the observed spectral line intensities with the calculated results. In Fig. 15 we show densitograms of the spectra radiated by laser plasma regions located at distances $x\simeq1-3$ mm from the target surface (dotted line), and the results of kinetic calculations for the chosen values of $N_e$ and $T_e$ (solid curve). The functions $N_e(x)$ and $T_e(x)$ measured in this way are shown in Fig. 16a. Note that in plasma regions close to the target ($x\leqslant0.3$ mm), the values of $N_e$ are calculated from the shape of the Al XII spectral lines, while the value of $T_e$ is obtained both from the ratio of the intensity of the resonance line of this ion to that of its dielectronic satellites, and from the intensity ratio of the $3p\ {}^2P-1s\ {}^2S$ line of Al XIII to the $1s7p\ {}^1P_1-1s^2\ {}^1S_0$ line of Al XII.

The functions $N_e(x)$ and $T_e(x)$ obtained in this way can be used to determine other parameters of the expanding laser plasma. For example, substituting them into the system of nonstationary kinetic equations enables us to track variations in the charge composition of the plasma as it disperses (a problem of high current interest in connection with the creation of laser injectors of multiply charged ions; see, e.g., Refs. 57, 58). Plots of the abundances of ions of various multiplicities obtained in this way are shown in Fig. 16b.

A second example comes from the study of $X$-pinch plasmas in regions far from the hot point. In experiments at the Cornell XP laboratory,[56,59] we observed that during the explosion of aluminum wires in the $X$-pinch geometry, the spectrum of the x rays from plasma regions located between the hot spot and the anode contained many spectral lines

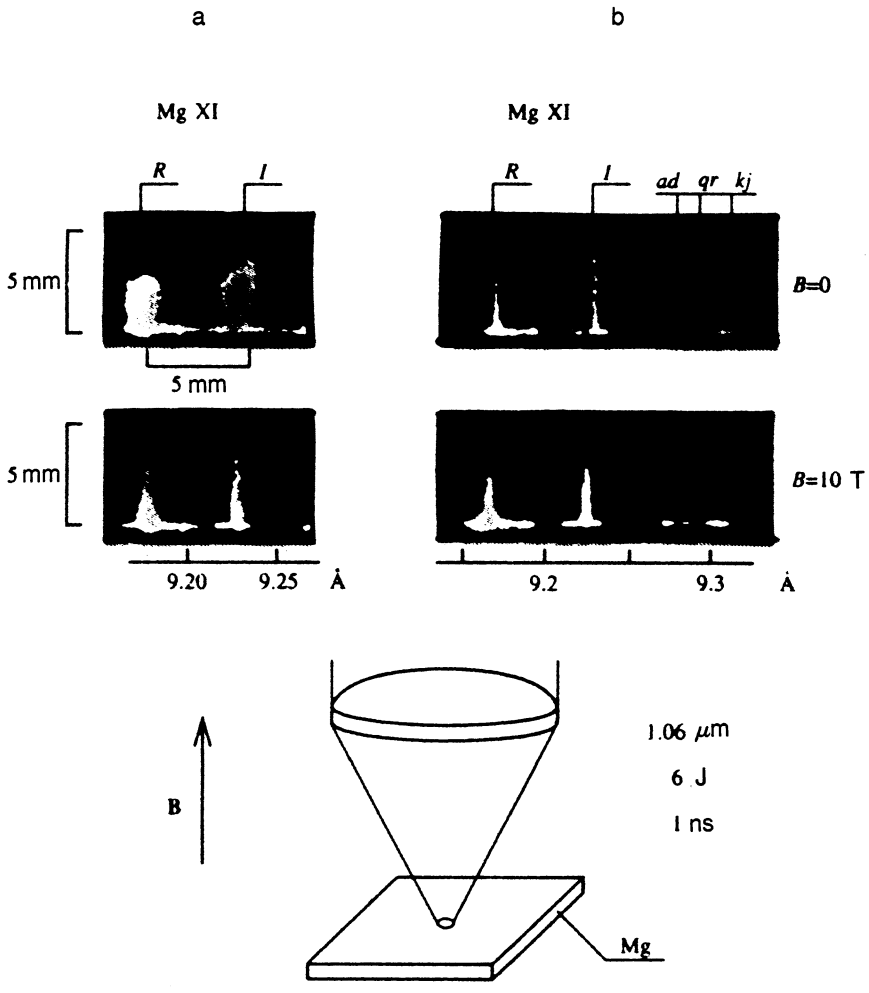


FIG. 18. Typical features of spectroheliogram near the $1s^2\ {}^1S_0-1s2p\ {}^1P_1$ resonance line of the He-like Mg XI ion during free expansion of a laser plasma, and during interaction with a 10-T axial magnetic field. a) FSPR-2 spectrograph, spherical mica crystal with $R=100$ mm; b) FSPR-1 spectrograph, spherical mica crystal with $R=100$ mm.

corresponding to radiative decay of $2p-1s$ autoionization states of Li-, Be-, B-, and C-like ions (see Fig. 17). Theoretical investigations[59] showed that excitation of these lines in these regions is attributable to the generation of an electron beam in the vacuum diode that arises as the hot spot at the $X$ pinch decays. Comparison of the experimental and computed values enables us to estimate both the plasma temperature in this region (which turned out to be $\simeq 30-80$ eV) and the electron beam density (of order $10^{-7}$ of the plasma density in this region, or $\simeq 10^{18}$ cm$^{-3}$).

### 4.3. High-resolution imaging spectroscopy for qualitative plasma diagnostics

There are a number of problems which, first and foremost, require information about the spatial structure of the plasma under study. In these cases, we can use the x-ray spectroscopic instruments with two-dimensional spatial resolution described in Sec. 2 above (FSPR-2; defocusing, focusing and Cauchois spectrographs with slits; and transmission diffraction gratings). If the images of centrosymmetric or axisymmetric objects are temporally resolved, subsequent mathematical processing enables us to obtain quantitative information about their spatial structure. If not, the results are more qualitative, although information of this kind sometimes turns out to have a considerable influence on our understanding of plasma processes.

We used spectrograms with two-dimensional spatial resolution—so-called spectroheliograms—to estimate the size and shape of plasmas. For example, in a freely expanding laser plasma, these spectroheliograms enable us to estimate the change in transverse dimensions of the plasma plume as it departs from the surface of the target. In Fig. 18, we show spectroheliograms of a laser magnesium plasma taken in both resonance and intercombination lines of the He-like Mg XI ion when the plasma was expanding freely (a), and expanding in an axial magnetic field with induction $B\simeq 10$ T (b).[42] In these spectroheliograms, the influence of the magnetic field on the structure of the laser plume is very clear: whereas in free expansion the plasma broadens into a cone with apex angle $\simeq 30°$, in the presence of an external magnetic field, a plasma jet formed at a distance $x\simeq 1$ mm from the target extends without broadening at least out to distances of approximately 5 mm with no appreciable reduction in luminosity.

The use of a spectrograph with spatial resolution makes it possible to study the spatial structure of x-ray sources, which is especially important in investigating complex plasma objects of the sort produced in experiments with the *Angara 5* accelerator (2 mA, 100 ns).[60] These experiments investigated the possibility of stabilizing a pinch when composite loads are used for the diode—specifically, in the compression of a hollow gas shell onto an axial wire load. De-

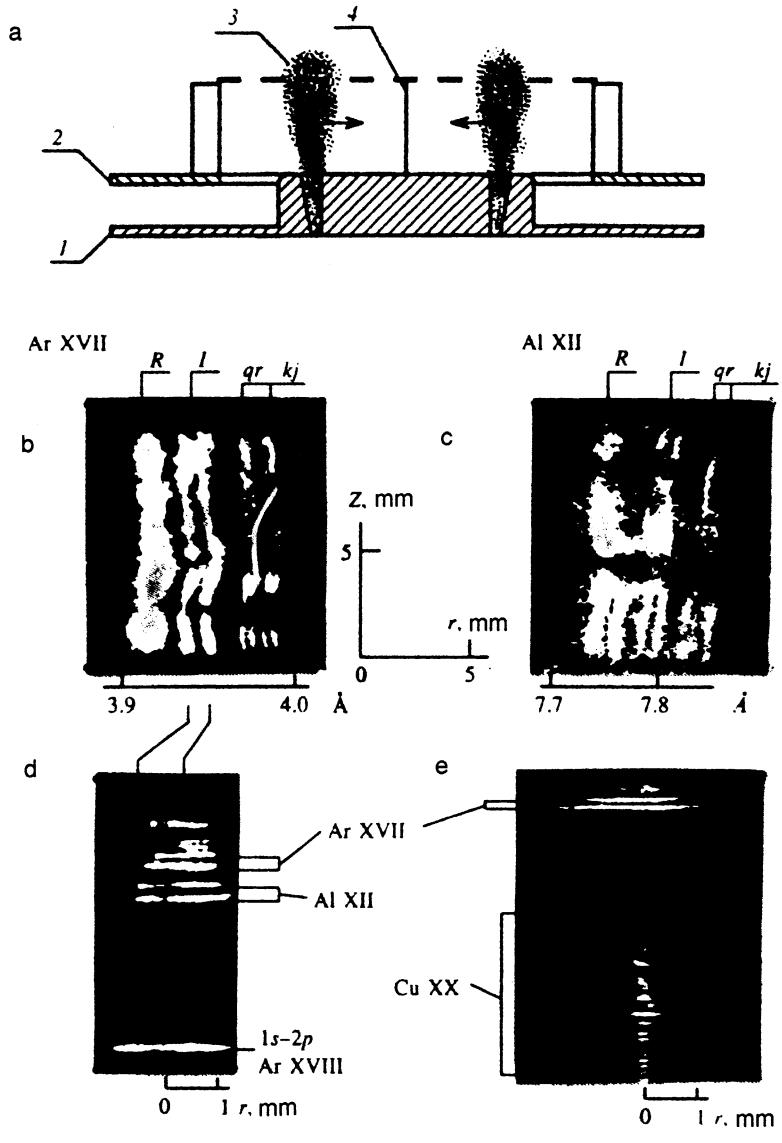


FIG. 19. Convex-crystal spectrographic images of a Z-pinch plasma with gas bleed and a wire load. a) Layout of diode and load. Two-dimensional images of plasma objects obtained using spectrograph with axial resolution, in the lines of b) Ar XVII (load: Ar plus $CD_2$ filament); c) Al XII (load: Al wire). Images of plasma objects obtained using a spectrograph with radial resolution, in the lines of d) Ar and Al (load: Ar plus Al wire); e) Ar and Cu (load: Ar plus Cu wire). *1, 2*—diode electrodes; *3*—gas jet; *4*—wire load.

tailed studies of the structure of the hot plasma formation is possible only when imaging spectrometers with one- or two-dimensional spatial resolution are used. The typical size of an object and its irregularities are of order tens (or even hundreds) of microns. Furthermore, it is bright, and emits over the spectral range from 3 to 15 Å. We were therefore able to investigate it with spectrographs that utilized convex mica crystals.

In these experiments, we investigated composite *Z* pinches with wire and gas loads (Fig. 19a). In several cases, the composition of the wire load was complex, e.g., palladium-clad copper wire, or an agar-agar cylinder with an admixture of NaCl or Mo. Often the composition of the gas shell was also complex, e.g., a mixture of Ne and Ar. In this case, using spectrographs in various orientations (see Sec. 2.1.1), we recorded spectra with spatial resolution along the axis and radius of the object, which we could use to identify precisely where and how the pinch occurs in the gas shell and the wire.

Figure 19 shows spectrograms of x rays from composite *Z* pinches with various loads, obtained by using a spectrograph with a convex mica crystal. It is clear from Figs. 19b and 19c, where we show two-dimensional images of the plasma produced by gas shell and wire, that the center of the load does not radiate (Fig. 19c), i.e., only the exterior expanding layer of the wire (which is pinched) is heated, precisely mimicking the structure of the gas jet (Fig. 19b). In Fig. 19e we show plasma spectrum from an argon *Z* pinch with a copper wire, from which it is clear that the pinching action of the argon shell takes place at a radius of 1 to 1.5 mm, whereas the copper wire, which exhibits essentially no free expansion (merely expanding from 20 to 300–400 $\mu$m), remains at the center of the target, where it is pinched and produces hot spots. When the wire load is made of material with lower *Z* than that of the gas jet (in our case, Ar and Al) (Fig. 19d), it expands out to roughly the same distance from the center of the pinch, i.e., 1–2 mm.

Our studies showed that there is no hot core in a complex *Z* pinch of this kind, and the plasma is heated out to distances of 1–2 mm from the axis of the object. It is likely that in the initial stage of the process, the diode current flows along the gas shell, heating and compressing it; there is also

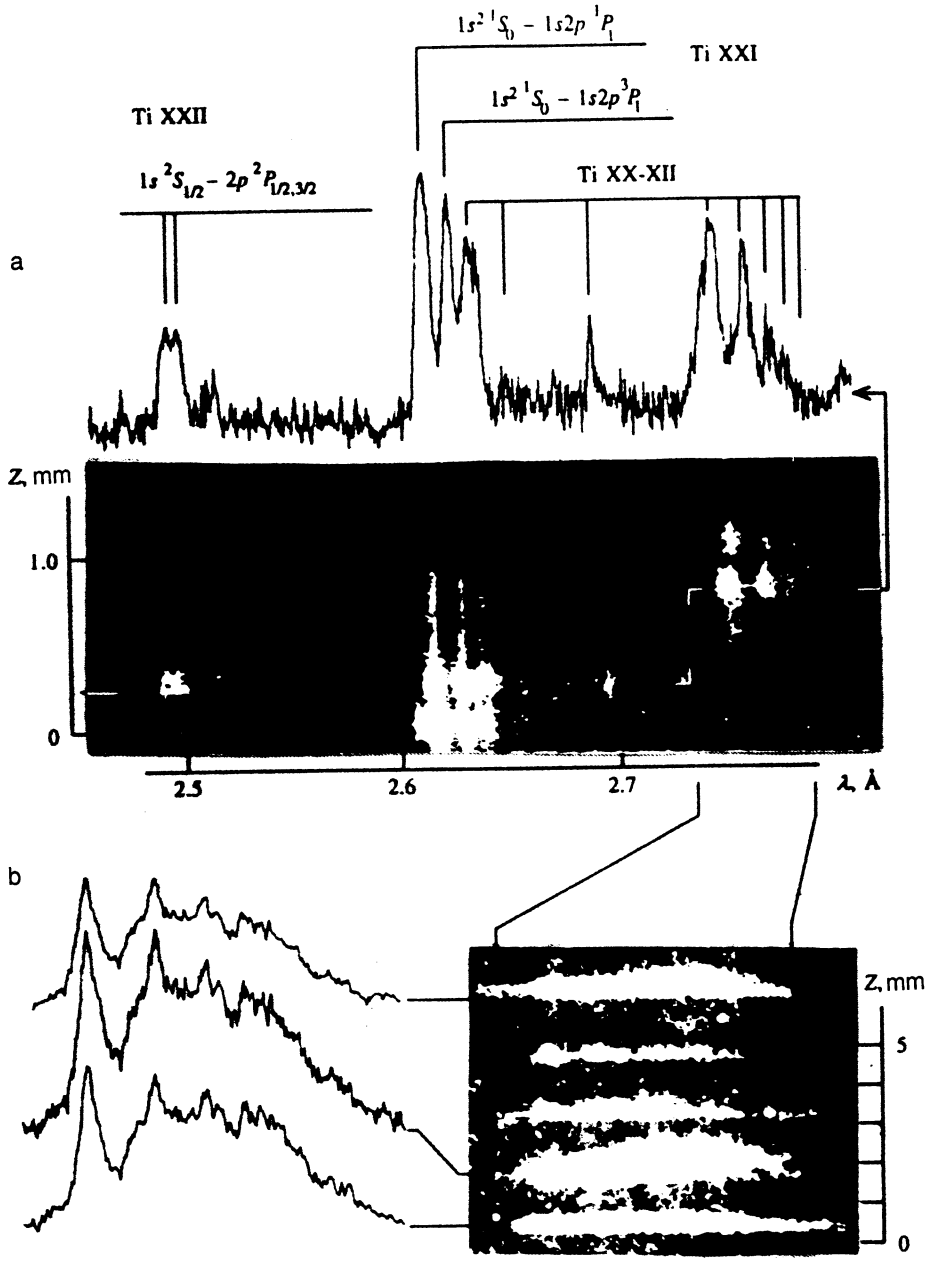


FIG. 20. a) Densitogram and image of a segment of the spectrum of H-like and He-like Ti ions in the plasma of an $X$ pinch recorded using a spectrograph with a convex mica crystal and a slit parallel to the crystal dispersion; b) densitograms and images of the spectrum near the $K_{\alpha 1}$, $K_{\alpha 2}$ lines recorded by an FSPR-1 spectrograph in the 7th reflection order of a mica crystal with radius of curvature $R = 250$ mm.

a slight heating and expansion of the wire under the action of emission from the shell plasma. When the two collide, the boundary layer between the shell and wire is heated, which also accounts for the identical structure of the shell and wire x rays.

The fine structure of $X$ and $Z$ pinches arising from the explosion of various types of wires (see Figs. 3 and 20–22) can be investigated similarly, i.e., by determining the number and size of hot spots, their ion content, temperature, and density. Figures 3b and 3c show spectrograms of $X$-pinch emission derived from Cu wires, obtained using a FSPR-1 spectrograph in a single shot. Using various orders of reflection from the mica, and x-ray films with various sensitivities, we were able to record images of the plasma in a single burst using the same spectrograph in fairly well-separated spectral regions. It is clear from these spectrograms that the emission from the cross of the $X$ pinch has a complex structure consisting of soft x rays from Ne-like copper ions (Fig. 3b), hard x rays from the $K_\alpha$ line of weakly ionized copper (Fig. 3c), and continuum x rays in the 3–6 Å, observed on both films. The continuum emission is typical of the most compressed regions of the plasma, i.e., individual hot spots roughly 20 $\mu$m across. Softer x-ray emission of Ne-like copper is observed near the hot spots out to about 100–200 $\mu$m, while $K_\alpha$ emission starts roughly 300–400 $\mu$m in the direction of the anode, and extends out to 3–4 mm or more. We see this sort of behavior in Figs. 3d and 3e, which show spectrograms of the emission from a Pd wire $X$ pinch.

In a $Z$ pinch, the structure of the emission from each hot spot is also complicated: we often record the spectra of both highly ionized ions and lines from the $K$ and $L$ series of weakly ionized ions in the emission from regions near an individual hot spot (Fig. 20b). Note that the regions emitting these lines are smaller than in an $X$ pinch (see Figs. 20a and

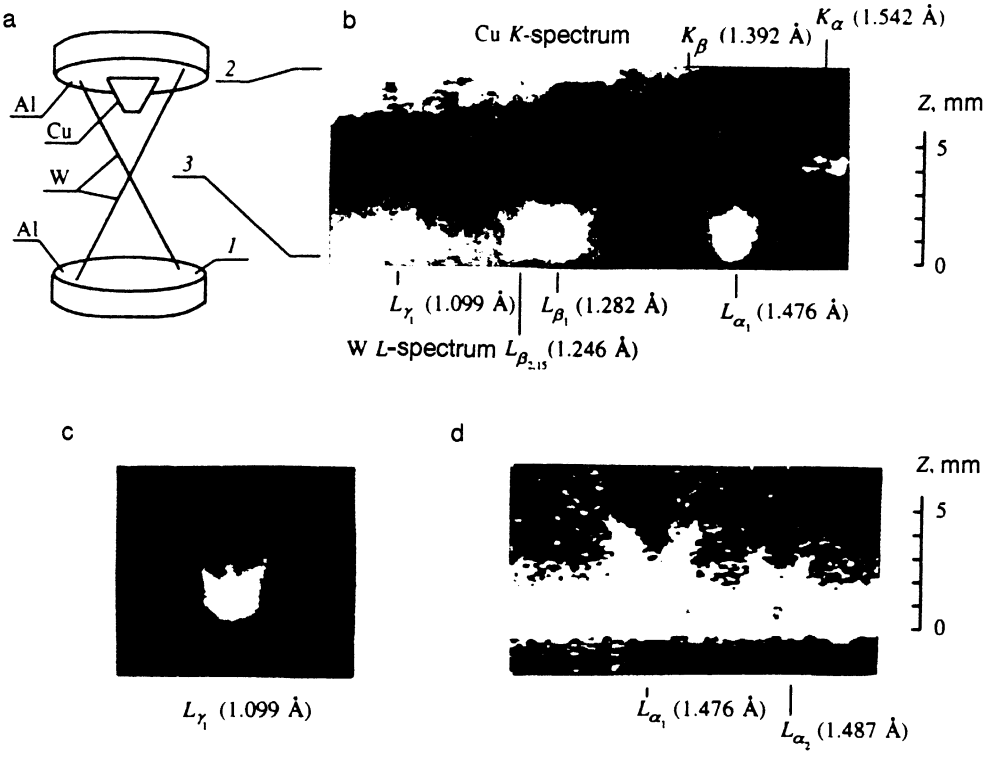


FIG. 21. a) Wire support in the *X*-pinch experiment. Images of x rays from an X-pinch plasma produced by tungsten wire, recorded with the following spectrographs: b) Cauchois, with a $(10\bar{1}1)$ quartz crystal with radius of curvature $R=250$ mm and slit in front of the crystal parallel to the crystal dispersion; c) x-ray microscope, mica crystal with radius of curvature $R=186$ mm; d) FSPR-2 spectrograph. *1*—cathode; *2*—anode; *3*—crossed wires of the *X* pinch.

20b). Spectrograms recorded with an FSPR-1 spectrograph from *X* and *Z* pinches involving light materials (Fig. 3a) exhibit notable expansion of the emitting plasma. As a rule, emission from the anode side is considerably weaker than from the cathode side. Using these lines, we can determine the plasma parameters both at the center of the pinch and its periphery. It is clear from these spectrograms that the heavier the wire material used to produce the *X* pinch, the weaker the plasma expansion observed in the emission lines of highly ionized ions, and the smaller the zone emitting in the continuum.

Previous investigations of the structure of plasmas in hard x rays used only camerae obscurae with filters. Only recently developed spectrographs with spatial resolution enable us to observe the structure of hard radiation in individual spectral lines. Figure 21 shows images of a plasma in various lines of the *L* spectrum of tungsten as recorded by various instruments.[34] In this experiment, to ease line identification and spatial calibration, we positioned a piece of copper foil at the anode (see Fig. 21a). The very fact that we detected lines of the tungsten *L* series indicates that an electron beam formed in the diode, and then generated the characteristic x rays of that series. If we possess spatially resolved spectra, we can thus determine the point at which the beam is generated—in the present case, the region where the wires cross. In a plasma pinch, an explosion takes place in the vicinity of this crossing. In essence, this is a miniature vacuum diode in which electrons are accelerated. The electron beam then interacts with the relatively cold plasma on the anode side of the *X* pinch, causing it to emit radiation. By spatially resolving this emission, we can observe the structure of the *X*-pinch plasma from the cross out to the anode. In Figs. 3 and 21, for example, we can see emission from the wires of the *X* pinch, and the plasma jet escaping from the cross in the direction of the anode. In Fig. 21b, emission from the copper foil is also evident in the $K_\alpha$ and $K_\beta$ lines of copper.

For certain problems, there is interest in investigating x rays at 20–100 Å, which does not fall within the "crystal" range. Techniques involving transmission diffraction gratings are exceedingly effective here, and we employed them to study the structure and estimate the absolute spectral density of plasma emission from fast *X* and *Z* pinches at 5–100 Å.

Figures 22b–22e illustrate several characteristics of images obtained with transmission diffraction gratings: a plasma pinch in an Ar+Ne gas jet (b) and exploding tungsten wires in the Z- (c) and *X*-pinch configurations (d,e). It is very clear that all of these have similar hot-spot structure (except that these hot spots are seldom very numerous for an *X* pinch; sometimes only one appears, at the point where the wires cross, as in Fig. 22d). In our experiments with *X* pinches, the maximum spectral energy density of the emission from hot spots, 2–8 J/Å, comes at 50–80 Å (for the *Z* pinch, this energy is distributed across several hot spots). The core region of the pinch, which is hotter and emits harder radiation ($\lambda\simeq 8$ Å), is an order of magnitude less intense (~0.3–1 J/Å). This probably results from differences not so much in the sizes of regions within the source that emit in different spectral ranges (from less than 10 $\mu$m for hard x rays with $\lambda<4$ Å to more than 1000 $\mu$m for soft x rays with $\lambda>20$ Å) as in the various "lifetimes" of the hot spots, which emit over a very brief interval ($\tau\leqslant 1$ ns), and of the more friable "corona," which exists (and emits) throughout the discharge, i.e., about 100 ns. Integration over the entire spectrum yields an estimate of the radiated spectral density, $I\simeq 1-2$ J/Å. We then find $W\simeq 10^7-10^8$ W/Å for the mean

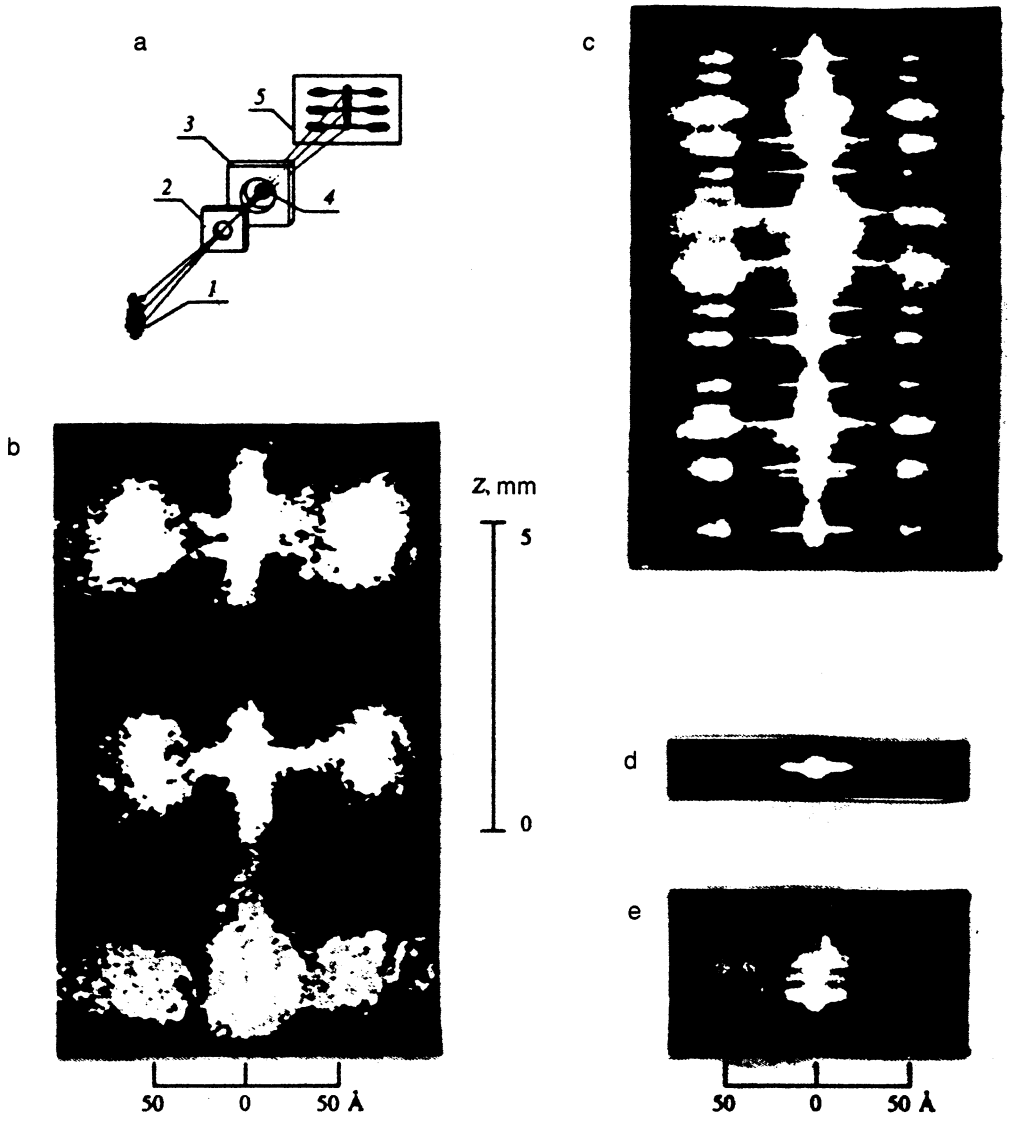


FIG. 22. Plasma object images obtained with a transmission diffraction grating. a) Optical layout of grating; b) plasma object in a Z pinch with gas bleed (mixture of Cr and Ne); c) plasma object in a tungsten-wire Z pinch; d, e) plasma object in a tungsten-wire X pinch with one (d) and several (e) closely-spaced "hot spots," respectively. *1*—x-ray source; *2*—entrance pupil in the form of an obscura; *3*—transmission grating aperture; *4*—tantalum transmission diffraction grating of diameter 25 $\mu$m and grating period 1 $\mu$m; *5*—plasma image.

TABLE VIII. Fundamental properties of an *X*-pinch, measured using X-ray imaging spectroscopy.

| Region | Size, mm | Density, cm | Temperature, eV | Time, ns | Spectral Range, Å | Energy, J |
|---|---|---|---|---|---|---|
| Wire framework | 0.05–0.2 | $10^{23}$ | 1 | 100 | – | – |
| Tenuous plasma | 1–10 | $10^{17}$–$10^{19}$ | 10–100 | 100 | 10–1000 | 100–500 |
| Jets | 1–3 | $10^{18}$–$10^{20}$ | 50–300 | 50 | 10–1000 | 10–100 |
| Dense plasma | 0.1–1 | $10^{20}$–$10^{22}$ | 100–700 | 10–30 | 3–100 | 10–300 |
| Hot spot | <0.02 | $> 10^{22}$ | >800 | < 5 | 1–10 | 1–10 |
| Electron beam | 1–2 | $10^{12}$–$10^{14}$ | >5000 | 2–10 | 0.1–2 | – |
| Ion beam | 1–2 | – | – | – | – | – |

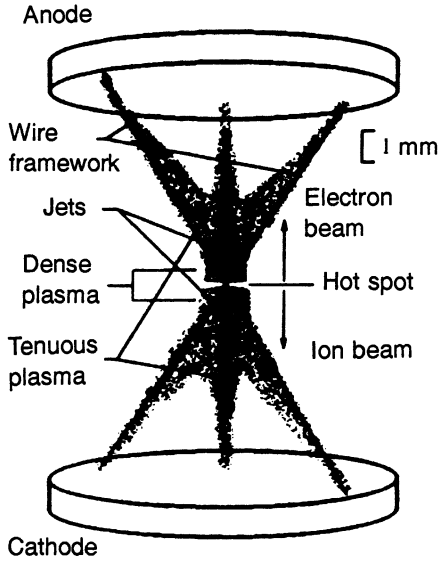


FIG. 23. Emission zones of an $X$ pinch, and a table of their fundamental characteristics measured by various x-ray imaging spectroscopy methods.

spectral power of our source. The intensity of the more diffuse emission from the gas jet, which occupies a larger volume, is approximately an order of magnitude lower.

Of course by using the full complement of x-ray spectrometers and diagnostic methods described above, we can obtain reasonably complete information about some arbitrary plasma object. For example, Fig. 23 shows the results obtained in this way in a study of $X$ pinches. Naturally, we cannot claim to have a complete description of the physics of an object as complex as a micropinch, but these data serve as a starting point in constructing a theory of the $X$ pinch, and in testing its implications.

## 5. CONCLUSION

In this study, we have shown that the emergence of a new class of instruments for x-ray imaging spectroscopy, which includes fast spectrographs with spherically curved crystals, transmission diffraction grating–obscurae and multilayer Bragg–Fresnel lenses, significantly enhances experimental spectroscopy of high-temperature plasmas. By using these instruments for atomic spectroscopy of multiply charged ions, we can more accurately measure the wavelengths of x-ray lines (primarily because emission spectra can now be recorded from relatively tenuous regions of the plasma, where line broadening is small) and investigate previously unobserved low-intensity spectral transitions.

With regard to plasma diagnostics, these instruments enable us to obtain information about spatial distributions of the plasma parameters (in one or two dimensions) of both nonuniform plasma micro-objects with linear dimensions $\leqslant 100$ $\mu$m (e.g., micropinches or dense regions of a laser plasma) and extended plasma sources in regions of low luminosity (e.g., freely expanding laser plasmas far from a target). In our opinion, further progress in this field will result from the amalgamation of such x-ray spectroscopic imaging instruments with recording instrumentation that provides high temporal resolution.

This work was partially financed by the Russian Fund for Fundamental Research, grant no. 93-02-15410, and the International Science Foundation, Grant no. MJB000.

[1] V. A. Boĭko, A. V. Vinogradov, S. A. Pikuz, I. Yu. Skobelev, A. Ya. Faenov, *X-Ray Spectroscopy of Laser Plasmas*, Itogi Nauki Tekhn., Ser. Radiotekhnika. Vol. 27, Moscow (1980); J. Sov. Laser Res. **6**, 85 (1985).
[2] E. V. Aglitskiĭ and U. I. Safronova, *Spectroscopy of Autoionization States of Atomic Systems* [in Russian], Energoatomizdat, Moscow (1985).
[3] V. A. Boĭko, V. G. Pal'chikov, I. Yu. Skobelev, and A. Ya. Faenov, *X Ray Spectroscopy of Multiply Charged Ions* [in Russian], Energoatomizdat, Moscow (1988).
[4] N. G. Basov, Yu. A. Zakharenkov, A. A. Rupasov, G. V. Sklizkov, and A. S. Shikanov, *Diagnostics of Dense Plasma* [in Russian], Nauka, Moscow (1989).
[5] R. C. Elton, *X-Ray Lasers*, Academic Press, New York (1990).
[6] E. V. Aglitskiĭ, V. V. Vikhrev, A. V. Gulov *et al.*, *Spectroscopy of Multiply Charged Ions in Hot Plasma* [in Russian], Nauka, Moscow (1991).
[7] B. A. Bryunetkin, S. A. Pikuz, I. Yu. Skobelev, and A. Ya. Faenov, Laser and Particle Beams **10**, 839 (1992).
[8] A. Ya. Faenov, Yu. A. Agafonov, B. A. Bryunetkin *et al.*, Proc. SPIE-93, 14–16 July 1993, San Diego **2015**, 64 (1993).
[9] T. A. Pikuz, B. A. Bryunetkin, A. Ya. Faenov *et al.*, Proc. SPIE-94, 24–29 July 1994, San Diego **2279** (1994).
[10] A. Ya. Faenov, S. A. Pikuz, A. I. Erko *et al.*, Physica Scripta **50**, 333 (1994).
[11] S. A. Pikuz, V. M. Romanova, T. A. Shelkovenko *et al.*, Kvant. Elektron. **22**, 21 (1995) [Quantum Electron. **25**, 16 (1995)].
[12] B. A. Bryunetkin, V. M. Dyakin, S. A. Pikuz *et al.*, Kvantovaya Elektronika **21**, 356 (1994) [Quantum Electron. **24** (1994)].
[13] E. Forster, K. Gabel, and I. Uschmann, Laser and Particle Beams **9**, 135 (1991).
[14] S. A. Pikuz, T. A. Shelkovenko, D. A. Hammer *et al.*, JETP Lett. **61**, 621 (1995).
[15] A. Ya. Faenov, S. A. Mingaleev, S. A. Pikuz *et al.*, Kvantovaya Elektronika **20**, 457 (1993) [Quantum Electron. **23**, 394 (1993)].
[16] M. Schnurer, P. V. Nickles, M. P. Kalashnikov *et al.*, Proc. SPIE-93, 14–16 July 1993, San Diego **2015**, 261 (1993).
[17] B. J. MacGowan, S. Maxon, L. B. Da Silva *et al.*, Phys. Rev. Lett. **65**, 420 (1990).
[18] V. V. Aristov and A. I. Erko, *X-Ray Optics* [in Russian], Nauka, Moscow (1991).
[19] A. G. Michette and C. J. Buckley, *X-ray Science and Technology*, IOP Publishing, London, 1993.
[20] B. A. Bryunetkin, G. V. Ivanenkov, S. A. Pikuz *et al.*, Pis'ma Zh. Tekhn. Fiz. **17**, 16 (1991) [Tech. Phys. Lett. **17**, 686 (1991)].
[21] S. A. Bel'kov, B. A. Bryunetkin, N. V. Zhidkov *et al.*, Kvantovaya Elektronika **21**, 271 (1994) [Quantum Electron. **24** (1994)].
[22] Yu. A. Agafonov, B. A. Bryunetkin, A. I. Erko, Kvantovaya. Elektron. **20**, 201 (1993) [Quantum Electron. **20**, 172 (1993)].
[23] A. I. Erko, L. A. Panchenko, S. A. Pikuz *et al.*, Rev. Sci. Instr. **66**, 1047 (1995).
[24] Yu. A. Agafonov, B. A. Bryunetkin, A. I. Erko, Pis'ma Zh. Tekh. Fiz. **18**, 56 (1992) [Tech. Phys. Lett. **18**, 533 (1992)].
[25] B. A. Bryunetkin, M. P. Kalashnikov, P. V. Nickles *et al.*, Kvantovata. Elektron. **20**, 393 (1993) [Quantum Electron. **23**, 337 (1993)].
[26] J. Abdallah, R. E. Clark, B. A. Bryunetkin *et al.*, Kvantovaya Elektron. **20**, 1159 (1993) [Quantum Electron. **23**, 1005 (1993)].
[27] B. A. Bryunetkin, V. M. Dyakin, J. Nilsen *et al.*, Kvantovaya Elektron. **21**, 142 (1994) [Quantum Electron. **24** (1994)].
[28] S. A. Pikuz, B. A. Bryunetkin, G. V. Ivanenkov *et al.*, JQRST **51**, 291 (1994).
[29] J. Nilsen, P. Beiersdorfer, S. R. Elliot *et al.*, Phys. Rev. A **50**, 2143 (1994).
[30] S. Ya. Khakhalin, V. M. Dyakin, A. Ya. Faenov *et al.*, Physica Scripta **50**, 106 (1994).
[31] B. A. Bryunetkin, A. Ya. Faenov, M. P. Kalashnikov *et al.*, JQRST **53**, 45 (1995).
[32] S. Ya. Khakhalin, V. M. Dyakin, A. Ya. Faenov *et al.*, J. Opt. Soc. Amer. (1995, in press).

[33] S. Bollanti, P. Di Lazzaro, F. Flora *et al.*, Physica Scripta **51** (1995, in press).
[34] S. A. Pikuz, V. M. Romanova, T. A. Shelkovenko *et al.*, Physica Scripta **51** (1995, in press).
[35] A. Ya. Faenov, D. A. Hammer, J. Nilsen *et al.*, Physica Scripta **51** (1995, in press).
[36] B. A. Bryunetkin, A. Ya. Faenov, S. Y. Khakhalin *et al.*, Kvantovaya Elektron. **22**, 205 (1995) [Quantum Electron. **25** (1995)].
[37] A. Ya. Faenov, I. Yu. Skobelev, S. A. Pikuz *et al.*, Phys. Rev. A (1995, in press).
[38] A. Ya. Faenov, B. A. Bryunetkin, V. M. Dyakin *et al.*, Phys. Rev. A (1995, in press).
[39] A. Osterheld, V. M. Dyakin, A. Ya. Faenov *et al.*, Phys. Rev. A (1995, in press).
[40] P. Beiersdorfer, "High-resolution studies of the x-ray transitions in highly charged states of neon-like ions on the PLT tokomak," Ph.D. Dissertation, Princeton University (1988).
[41] S. MacLaren, P. Beiersdorfer, D. A. Vogel *et al.*, Phys. Rev. A **45**, 329 (1992).
[42] V. M. Dyakin, A. Ya. Faenov, I. Yu. Skobelev *et al.*, Kvantovaya Elektron. **21**, 1186 (1994) [Quantum Electron. **24** (1994)].
[43] V. M. Dyakin, A. Ya. Faenov, A. I. Magunov *et al.*, Physica Scripta (1995, in press).
[44] V. A. Boĭko, V. G. Pal'chikov, I. Yu. Skobelev, and A. Ya. Faenov, *Spectroscopic Constants of Atoms and Ions (Spectra of Atoms with One and Two Electrons)*, Standarty, Moscow (1988).
[45] P. Beiersdorfer, S. R. Elliot, and J. Nilsen, Phys. Rev. A **49**, 3123 (1994).
[46] G. A. Kyrala, R. D. Fulton, K. K. Wahlin *et al.*, Appl. Phys. Lett. **60**, 2195 (1992).
[47] L. A. Vainshtein and U. I. Safronov, Preprint No. 6, Institute of Spectroscopy, USSR Acad. Sci. (1985).
[48] L. A. Vainshtein and U. I. Safronov, "Correlation and relativistic effects in atoms and ions," in *Council on Spectroscopy*, USSR Acad. Sci., Moscow (1986), p. 190.
[49] J. Nilsen, Data and Nuclear Data Tables **41**, 131 (1989).
[50] M. Klapisch, J. L. Schwob, B. S. Fraenkel, and J. Oreg, J. Opt. Soc. Amer. **67**, 148 (1977).
[51] J. Oreg, W. H. Goldstein, M. Klapisch, and A. Bar-Shalom, Phys. Rev. A **44**, 1750 (1991).
[52] S. A. Pikuz, B. A. Bryunetkin, G. V. Ivanenkov *et al.*, Kvantovaya Elektron. **20**, 237 (1993) [Quantum Electron. **23**, 202 (1993)].
[53] B. A. Bryunetkin, I. Yu. Skobelev, A. Ya. Faenov *et al.*, Kvantovaya Elektron. **20**, 619 (1993) [Quantum Electron. **23**, 537 (1993)].
[54] S. A. Pikuz, V. M. Romanova, T. A. Shelkovenko *et al.*, "Spectroscopic Investigations of the X-ray Spectra from *X*-Pinch Plasmas," Proc. 10th Intl. Conf. on High-Power Particle Beams "Beams-94," San Diego, 20–25 June, 1994.
[55] A. Vartnik, V. M. Dyakin, P. Paris *et al.*, Kvantovaya Elektron. **22**, 25 (1995) [Quantum Electron. **25** (1995)].
[56] S. A. Pikuz, D. A. Hammer, D. H. Kalantar *et al.*, Phys. Rev. A **49**, 3450 (1994).
[57] Y. Amidouche, H. Haseroth, A. Kuttenberger *et al.*, Preprint CERN-PS 91-48 (HI) (1991).
[58] W. Mroz, J. Wolowski, E. Woryna *et al.*, Rev. Sci. Instr. **65**, 1272 (1994).
[59] J. Abdallah, Jr., A. Faenov, D. Hammer *et al.*, Phys. Rev. E (1995, in press).
[60] A. N. Batunin, A. V. Branitsky, I. N. Frolov *et al.*, *Proc. 3rd Intl. Conf. on Dense Z Pinches*, London (1993), p. 580.
[61] V. Kaufman and W. C. Martin, J. Chem. Phys. Ref. Data **20**, 777 (1991).

Translated by Frank Crowne